A dynamic and spatially periodic micro-pattern of HES5 expression underlies the probability of neuronal differentiation in the mouse spinal cord

Biga V[1]*, Hawley J[1]*, Johns E[1], Han D[2], Kursawe, J[3], Glendinning P[2], Manning C.S[1]*#. and Papalopulu N#[1]

[1] Faculty of Biology Medicine and Health, The University of Manchester, Oxford Road, Manchester, M13 9PL, UK

[2] Department of Mathematics, School of Natural Sciences, Faculty of Science and Engineering, The University of Manchester, Oxford Road, Manchester, M13 9PL, UK

[3] School of Mathematics and Statistics, University of St Andrews, St Andrews, KY16 9SS, UK.

Corresponding authors

* These authors have contributed equally to this work.

VB, JH and CSM contributed equally.

CSM and NP contributed equally.

Short title: HES5 micro-patterns explain rate of neurogenesis

Abstract

Some regulatory transcription factors (TFs), such as the Helix-loop-Helix TF, HES5, show dynamic expression including ultradian oscillations, when imaged in real time at the single cell level. Such dynamic expression is key for enabling cell state transitions in a tissue environment. In somitogenesis, such expression is highly synchronised in blocks of tissue (somites), however, in neurogenesis it is not known how single cell dynamics are coordinated, the multiscale pattern that emerges and the significance for differentiation. In this study, we monitor the expression of HES5 protein ex-vivo in the developing spinal cord and identify the existence of microclusters of HES5 expressing progenitors that are spatially periodic along the dorso-ventral (D-V) axis and that in addition are temporally dynamic. We use multiscale computational modelling to show that such microclusters arise at least in part from local synchronisation in HES5 levels between single cells mediated by Notch-Delta interactions. We find that the HES5 microclusters are less dynamic in the presence of a Notch inhibitor showing that Notch mediated cell-cell communication is required for temporal characteristics. Moreover, predictions from the computational modelling and experimental data show that the strength of interaction between neighbouring cells is a key factor controlling the rate of differentiation in a domain specific manner. Our work provides evidence of co-ordination between single cells in the tissue environment during the progenitor to neural transition and shows the functional role of complexity arising from simple interactions between cells.

(267 words)

Key findings

- HES5 is expressed in microclusters that are spatially periodic along the dorsal-ventral axis in mouse spinal cord and are also dynamic in the temporal domain.
- Notch signalling maintains the temporal characteristics of the pattern.
- Based on dynamic data and computational modelling, microclusters can arise from single cell oscillators that are weakly coupled via Notch.
- Computational modelling predicts that the spatial pattern and the probability for progenitor differentiation is regulated by the coupling strength between cells.

- Motorneuron progenitor domain has higher rate of differentiation than interneuron progenitor domain and a spatial pattern of HES5 more similar to a checker-board type salt-and-pepper pattern, corresponding to a higher coupling strength.

Overall: Periodic HES5 micro-patterns can be generated by local synchronisation of low coherence single cell oscillators present in spinal cord tissue and these patterns are maintained in a dynamic way through Notch mediated cell-cell interactions. A computational model predicts that coupling strength changes spatial patterns of expression and in turn, the probability of progenitor differentiation. We confirm that between adjacent progenitor domains in the spinal cord, the rate of differentiation correlates with spatial patterns of HES5.

Introduction

Neurogenesis is the developmental process which generates the variety of neuronal cell types that mediate the function of the nervous system. Neurogenesis takes place over a period of days during mouse embryogenesis, thus, the transition from progenitor maintenance to differentiation needs to be balanced for development to occur normally. Neurogenesis relies on the integration of positional information with the transcriptional programme of neuronal differentiation. In the spinal cord, notable progress has been made in understanding the role and regulation of the dorso-ventral (D-V) positional system, that relies on secreted morphogens and transcriptional networks to generate the stereotyped array of different types of neurons along this axis (Briscoe & Small, 2015; Sagner & Briscoe, 2019). The transcriptional programme that mediates neurogenesis is also well understood in the spinal cord, particularly with the application of single cell sequencing (Delile *et al*, 2019; Paridaen & Huttner, 2014; Sagner & Briscoe, 2019).

Recent live imaging studies of cell fate decisions during neurogenesis have added a new dimension to this knowledge (Das & Storey, 2012, 2014; Manning *et al*, 2019; Nelson *et al*, 2020; Soto *et al*, 2020; Vilas-Boas *et al*, 2011). They have shown the importance of understanding transcription factor (TF) expression dynamics in real time, including the key transcriptional basic helix-loop-helix repressors Hairy and enhancer of split (HES)1 and 5 (Bansod *et al*, 2017; Imayoshi & Kageyama, 2014; Ohtsuka *et al*, 1999), in regulating state transitions. We have previously shown that in spinal cord tissue, HES5 exhibits ultradian periodicity of 3-4h in about half of the progenitor population with the remaining progenitors showing aperiodic fluctuations (Manning *et al.*, 2019). The percentage of cells that show oscillations rises in cells that enter the differentiation pathway; such cells show a transient phase of more coherent oscillations before the level of HES5 is downregulated in differentiated cells (Manning *et al.*, 2019). Furthermore, our studies of a zebrafish paralogue Her6 showed that the transition from aperiodic to oscillatory expression is needed for neuronal differentiation, suggesting that oscillatory expression has an enabling role for cell state transitions (Soto *et al.*, 2020) as we have previously predicted computationally (Bonev *et al*, 2012; Goodfellow *et al*, 2014; Phillips *et al*, 2016).

Although these studies revealed an unappreciated dynamic behaviour at the level of HES TF protein expression, these live imaging studies are based on recording dynamics from sparsely distributed single cells in the tissue context. Therefore, little is known about how single cell dynamics are synthesised to tissue level dynamics. Do cells interact with their

neighbours in order to coordinate their cell state transitions and if so, how and what is the mechanism?

Notch is of particular interest in this context because it is a highly conserved cell to cell signalling pathway that is well known for generating complex spatial patterns of cell fates in tissue development (Cohen *et al*, 2010; Corson *et al*, 2017; Henrique & Schweisguth, 2019; Hunter *et al*, 2016; Shaya & Sprinzak, 2011). Activation of Notch receptors by Notch ligands, including DLL1 and JAG1, results in downstream expression of HES1 and HES5. HES TFs can influence Notch activity on neighbouring cells by repressing Notch ligand expression either directly (de Lichtenberg *et al*, 2018; Kobayashi *et al*, 2009) or indirectly through the repression of proneural TFs such as NGN1/2 (Ma *et al*, 1998). We argue that in order to understand how the balance of progenitor factor HES can be tipped in favour of a proneural factor giving rise to a decision point in neural progenitor cells, we need to address tissue-level patterns of HES expression and use computational models that can integrate the complexity of interactions at multiple scales.

The effects of Notch-Delta signaling combined with HES oscillations have been investigated during somitogenesis. Live imaging of dissociated PSM cells in vitro has shown that single cell oscillators can self-organise through Notch dependent synchronisation to generate waves in gene expression similar to those observed in vivo (Tsiairis & Aulehla, 2016). A model of mRNA and self-repression with transcriptional delay explains the emergence of autonomous oscillations of Her1 and Her7 as well as synchronization by Notch activity as observed during the formation of somites (Lewis, 2003; Özbudak & Lewis, 2008; Webb *et al*, 2016). A more abstract Kuramoto-style model with time delays explains how a population of initially asynchronous and autonomous oscillators can evolve to adopt the same frequency and phase in order to periodically form somites (Morelli *et al*, 2009; Oates, 2020). The period of the oscillations determines the size of the somite and Notch abundance controls dynamic parameters such as the time to synchronisation (Herrgen *et al*, 2010). Apart from a limited number of studies suggesting an anti-phase relationship of DLL1 oscillations in neighbouring cells in neural cells (Shimojo *et al*, 2016), whether and how neural progenitor cells co-ordinate fate decisions and dynamic HES activity with their neighbours remains unknown.

In this study, we hypothesise that the spatial co-ordination between HES5 expressing progenitors is important for the decision point and in turn for the transition towards differentiation. In the mouse spinal cord, we find that HES5 expression is locally positively correlated between nuclei in microclusters. Microclusters are periodic in space along the dorso-ventral axis of the spinal cord with spatial periodicity of approximately 4 cells. These micropatterns are dynamic such that the gene expression in one region can fluctuate over

time between low and high levels of HES5 and this is dependent on Notch signalling. We use a multiscale model combining the principles of single cell oscillations and Notch-Delta receptor-ligand interactions between cells to show that coupled oscillators with weak local synchronisation can generate microclusters of HES5 expression, although additional factors/mechanisms may be needed to increase the occurrence and spatial periodicity of the microclusters. Furthermore, the model predicts that the strength of the Notch-Delta interaction can influence the type of spatiotemporal HES5 pattern and the probability of progenitor differentiation. We confirm that the motorneuron (MN) domain, which has a greater rate of differentiation than the ventral interneuron (IN) domain, has a different spatial HES5 pattern with periodic arrangement of single cells in alternating high and low states, corresponding to a salt-and-pepper pattern. Thus, this is an exquisite spatiotemporal mechanism conferring tissue level regulation of the transition of single cells from neural progenitor to neuron.

Results

Microclusters of spinal cord progenitor cells have positively correlated HES5 levels

HES5 is expressed in two broad domains in the dorsal and ventral embryonic mouse spinal cord (Manning *et al.*, 2019; Sagner *et al*, 2018). Previously we have characterised the single cell dynamic behaviour of the more ventral HES5 expression domain that covers the ventral interneuron (p0/p2) and motorneuron progenitors (p2/pMN) (Manning *et al.*, 2019). Thus, to understand how the single cell expression dynamics contributes to tissue level behaviour we have focused here on the same ventral area of HES5 expression (**Figure 1** and **Supp. Fig 1a**). In this area, all progenitor cells (marked by SOX2) show HES5 expression (**Supp. Fig. 1b).** To characterise the spatial pattern of HES5 protein expression in this progenitor domain we made ex-vivo slices of E10.5 Venus::HES5 knock-in mouse embryo spinal cord (Imayoshi *et al*, 2013). In snapshot images of this domain we noticed multiple local clusters of neural progenitor cells with similar levels of nuclear HES5 (**Figure 1a**). These 'microclusters' are notable after manual segmentation using a Draq5 live nuclear stain and averaging HES5 intensity across the nucleus (**Figure 1a-c**)**.** The differences in Venus::HES5 intensity between nuclei did not correlate with the Draq5 nuclear staining indicating this was not related to global effects or effects of imaging through tissue (**Supp. Fig. 1c**). By measuring the number of nuclei in microclusters with high Venus::HES5 levels we found that they consisted of 2-3 cells wide in the dorso-ventral direction and 3-4 cells wide in the apical-basal direction (**Figure 1d**). Consistent with the presence of microclusters of cells with similar levels, nuclei showed a positive correlation in Venus::HES5 between neighbours 1 to

4 (**Figure 1e**). We took a more quantitative approach and correlated mean nuclear HES5 levels between all pairs of nuclei and found that nuclei close to each other were highly positively correlated and this correlation dropped with increasing distance, becoming negative at distances over 50 µm (**Figure 1f** and **Supp. Fig. 1d**). This pattern was substantially different to the correlation coefficients calculated from randomisations of the nuclei intensities but keeping the same nuclear spatial arrangement (**Figure 1f**), which indicates the presence of a pattern in HES5 levels.

The longer-range negative correlations may arise from gradients in HES5 expression in apical-basal (A-B) and D-V direction seen in nuclear HES5 intensity representations of the whole domain (**Figure 1g, Supp. Fig. 1d** and (Manning *et al.*, 2019)). Indeed, plotting the HES5 intensity as a function of distance from a centre of high HES5 expression, follows the same shape as a theoretical radial gradient of expression (**Figure 1h**), emanating from areas of highly expressing cells. Such a radial gradient could be due to the downregulation of HES5 as cells differentiate and move basally from the progenitor domain as well as to D-V differences in the level of expression (see below), and is not further investigated here. To ask whether the local positive correlations in HES5 levels are an artefact of this larger-scale domain expression pattern, we measured and subsequently removed a radial gradient across the tissue from the segmented single cell images. However even after removing a radial gradient, mean nuclear HES5 levels remained highly positively correlated at distances less than 40-50 µms (**Figure 1i** and **Supp. Fig. 1g**). Therefore, a radial gradient cannot fully explain the HES5 spatial pattern and further factors, such as microclusters of cells with similar HES5 levels, must contribute to the formation of the HES5 spatial pattern.

HES5 microclusters are spatially periodic along dorso-ventral axis of spinal cord

The high-resolution analysis of single-cell snapshots showed the presence of multiple microclusters in HES5 expression in the ventral domain. Next, we asked whether these microclusters have a regular spatial arrangement. To do this we drew line profiles 15 µm wide, parallel to the ventricle, in the ventral to dorsal direction **(Figure 2a** and **Supp. Fig 2a,b)** and plotted the Venus::HES5 intensity along this line from lower resolution 20x images of ex-vivo slice cultures **(Figure 2b)**. Throughout the paper the 0 distance is the ventral most point of the HES5 domain, and distance extends dorsally **(**Materials and Methods). Detrending the signal removed a ventral-to-dorsal bell shape of expression that is a result of different HES5 levels along the D-V axis and is not further investigated here (**Figure 2b**). The microclusters could be detected as peaks in the detrended Venus::HES5 intensity profile and we observed multiple peaks across the D-V axis (**Figure 2c**). Periodicity analysis

of the detrended spatial Venus::HES5 expression profile revealed the presence of significant peaks in the power spectrum (**Figure 2d**) and multiple significant peaks in the auto-correlation function (**Figure 2** and **Supp. Fig. 2c**). Multiple peaks in an autocorrelation function are indicative of a periodic signal with the peak-to-peak distance in the autocorrelation corresponding to the period of the signal. In this case, there was a spatial period in Venus::HES5 expression of 30 µm to 60 µm with a median period of 40 µm.

To understand how our observed spatial periodicity relates to nuclear count in the tissue, we analysed the spatial profile for the Draq5 nuclear stain from snapshot images of Venus::HES5 ex-vivo slices. We observed peaks in Draq5 in regions of low Venus::HES5 indicating that the lower Venus::HES5 regions did not correspond to a lack of nuclei at this position of the tissue (**Supp. Fig. 2a,b**), excluding co-ordinated Interkinetic Nuclear Migration as the explanation for the spatial periodicity in expression. As expected, the Draq5 signal observed along the D-V axis also showed multiple significant peaks in the autocorrelation that corresponded to a spatial period of 10 µm, a single-cell width (**Figure 2f** and **Supp. Fig. 2c,d**). Using this value we estimate that the periodic occurrence of microclusters of cells with correlated levels of Venus::HES5 has a median period of 4 cells.

Since the apical region of spinal cord contains proliferative neural progenitors with high levels of HES5 that become downregulated when progenitors begin to migrate towards basal regions, we interrogated if the spatial periodicity persisted in the apical to basal axis. Venus::HES5 expression profiles collected from apical, intermediate and basal regions (**Figure 2g**) within the HES5 expression domain all showed spatial periodicity with the period varying from approximately 4 cells in the apical side to 3 cells in the basal region (**Figure 2h,i** and **Supp. Fig. 2e**). These results suggest that proliferative progenitors (localised apically) as well as differentiating progenitors (localised more basally) show local spatial correlation in Venus::HES5 levels between neighbouring cells where 2-6 neighbouring cells can be in a high or low state in synchrony with each other and that these clusters are repeated periodically in the D-V axis.

The HES5 spatial pattern is dynamic over time

We next investigated whether the spatially periodic pattern in Venus::HES5 is also dynamic over time. To do this, we generated kymographs by drawing a 15 µm wide line in the ventral to dorsal direction in movies of E10.5 Venus::HES5 spinal cord ex vivo slices **(Figure 3a**, **Supp. Movie 1** and see Methods). We noticed stripes in the kymograph, corresponding to the spatially periodic Venus::HES5 pattern (**Figure 3b**). To investigate how long high HES5

and low HES5 clusters persist over time we split the kymograph into adjacent 20 μm regions along the D-V axis and followed their levels over time. Hierarchical clustering of the dynamic behaviour of these regions revealed changes from low to high Venus::HES5, high to low, or fluctuations between the two states, showing that clusters of cells can interconvert between low and high HES5 states (**Figure 3c**). The persistence of a cluster in the "on" or "off" state was 6-8 hours with no significant difference between persistence of high or low states (**Figure 3d-e**).

Since the HES5 expression is periodic along the D-V axis, it can be represented as a spatial oscillator. Therefore, we used its phase characteristics denoting the position in the spatial cycle, to analyse how the HES5 signal changes from high to low in the same region over time. We transformed the detrended spatial Venus::HES5 intensity (**Figure 3f**) along the D-V axis to phase of the spatial oscillator of Venus::HES5 (**Figure 3g,h)** using the Hilbert transform (Methods). All experiments showed a highly dynamic pattern with multiple changes in phase in any one position of the tissue in the 12 to 24 hr movies (**Suppl. Fig. 3a-c**). Regions could be identified that maintained a similar phase over time followed by a change, indicating a switch in state of the Venus::HES5 pattern. Phase waves could be observed in some movies (**Suppl. Fig 3a-iii**), indicated by the diagonal lines of similar colours in the spatial phase map, however these did not have a consistent direction in the D-V axis between experiments. In summary, we find microclusters of cells with correlated Venus::HES5 levels that are a maximum of 2-3 cells wide in D-V and 3-4 in A-B axes and are arranged in a spatially periodic pattern. The pattern is also temporally dynamic with a persistence of 6-8 hrs but no consistent phase wave travel in D-V.

Notch inhibition extinguishes HES5 levels and spatial pattern through amplitude death and spatial period increase

We hypothesised that the periodic microclusters of HES5 are generated through Notch-Delta interactions that locally synchronise dynamic HES5 expression between neighbouring cells. To test this, we treated spinal cord slice cultures with the Notch inhibitor DBZ. In Notch inhibitor conditions, the HES5 levels reduce continuously over time (**Figure 4a**) and the amplitude of the HES5 spatial pattern appears diminished compared to control DMSO treated conditions (**Figure 4b**). These effects indicate that the DBZ is effective and cell-to-cell communication through Notch is significantly reduced. We performed kymograph analysis in the apical region of DMSO and DBZ treated spinal cord ex-vivo slices. Spatial periodicity could be detected at the start of the movie, immediately after DBZ addition, however the spatial periodicity was gradually extinguished through amplitude death (**Supp.**

Fig. 4a). Approximately 45% of the DBZ treated slices did not show significant peaks in the auto-correlation of detrended spatial Venus::HES5 profile by 10-12 hrs of treatment (**Figure 4c**) whereas periodicity was maintained in all DMSO conditions. Spatial periodicity in detrended Venus::HES5 levels that could be detected in DBZ treatment at early time points frequently appeared higher in Notch inhibitor treated ex-vivo slices than in DMSO control (**Figure 4d** and **Supp. Fig. 4b**). Cell density also decreased in Notch inhibitor conditions suggesting this increase in spatial period was partially due to changes in the spatial arrangement of cells (**Supp. Fig. 4c**).

We next turned our attention to the spatiotemporal characteristics of the HES5 pattern in the presence of Notch inhibition and investigated detrended HES5 and corresponding phase characteristics. We observed that the temporal transitions of microclusters of cells from high to low Venus::HES5 were impaired by DBZ and as a result fewer changes in the phase of the spatial periodic Venus::HES5 pattern occurred indicating the spatial pattern remained stable (**Figure 4e,f** and **Supp. Fig 4d,e**). This was quantified with a phase synchronisation index (see Methods), where low values indicate multiple phase changes at specific D-V locations **(Figure 4g)**. The phase synchronisation index was significantly higher in DBZ treated tissue indicating that in the absence of Notch signalling, HES5 microclusters were more persistent in the same region and that the dynamic changes in Venus::HES5 microclusters between high and low levels are mediated by Notch signalling.

Taken together, these findings show that Notch signalling is responsible for certain aspects of the pattern, such as the dynamic switching between high/low HES5 microcluster states over time. However, inhibition of Notch does not seem to abolish the existence of microclusters or their spatial periodicity, as they can still be detected until amplitude death occurs and the HES5 levels are depleted.

A model of Notch-Delta with HES5 auto-repression containing stochasticity and delays explains the existence of HES5 microclusters

We used computational modelling to help us understand how positively correlated, spatially periodic, and dynamic microclusters of cells may emerge in the spinal cord. At single cell level, HES5 protein expression oscillations are due to HES5 self-repression, an intra-cellular transcriptional time delay (τ_H) and short protein and mRNA half-lives (Jensen *et al*, 2003; Momiji & Monk, 2008; Monk, 2003). We represented the auto-repressive interactions between HES5 mRNA and protein using stochastic differential equations with time delay, as previously described in (Galla, 2009; Manning *et al.*, 2019; Phillips *et al.*, 2016). This single

cell model has been shown to faithfully recapitulate statistics of single cell HES5 expression dynamics collected from spinal cord tissue (Manning *et al.*, 2019). Given that Notch signalling can maintain groups of positively correlated neighbouring cells in a dynamic state (above), we extended the single-cell mathematical description of HES5 to a coupled dynamical model by incorporating a repressive interaction in the form of a Hill function, that describes how HES5 protein in one cell represses Hes5 transcription in a neighbouring cell via Delta-Notch signalling **(Figure 5a** and **Supp. Fig 5a)**. We introduce the following set of inter-cellular parameters (**Figure 5b** and Materials and Methods): (i) *inter-cellular time delay*, representing the time required to transfer the signal from one cell to another, that is, the time required for a change in HES5 protein in one cell to affect Hes5 transcription in a neighbouring cell through Notch-Delta; (ii) *the inter-cellular repression threshold,* representing the amount of HES5 protein required to reduce Hes5 transcription in a neighbouring cell by half; the inter-cellular repression threshold is inversely proportional to coupling strength where higher coupling strength (or low inter-cellular repression threshold) indicates that less protein is needed to repress the neighbour's Hes5 transcription by 50%; and (iii) *inter-cellular Hill coefficient* indicating how steep the response curve of Hes5 transcription is in response to a change in HES5 protein in the neighbouring cell, with higher values corresponding to increased nonlinearity. Interactions between cells are considered in a hexagonal grid whereby each cell can interact with its immediate 6 neighbours and repression between cells is calculated through the inter-cellular Hill function by averaging HES5 protein abundance over 6 neighbours (**Figure 5b,c** and Materials and Methods). Thus, we generated a comprehensive, multiscale and stochastic model with time delays, representative of the Delta-Notch-Hes interactions in the multicellular tissue environment.

We parameterised this multiscale HES5 model with previously determined experimental measures of HES5 protein and mRNA stability and with parameter values of the single cell HES5 self-repression loop that can reproduce single neural progenitor HES5 dynamics (see Methods and **Supp. Table 1** Main), as identified through Bayesian inference in our previous work (Manning *et al.*, 2019). We then investigated the parameter space of unknown model parameters that are characteristic of cell-to-cell interactions, namely the repression threshold (inverse of coupling strength) and time delay, to identify values that are compatible with the temporal period and phase synchronisation level of single cell Venus::HES5 expression dynamics **(Figure 5d,e)**. The mean temporal period of Venus::HES5 in ex-vivo spinal cord tissue is approx. 2-6 hrs (mean 3.3 hrs) (Manning *et al.*, 2019), which could be reproduced by the model in a wide range of coupling strength and inter-cellular time delay values (**Figure 5d,f**). The temporal phase synchronisation between single Venus::HES5 expressing cells was measured with the Kuramoto order parameter (KOP, also known as mean field

value (Choi *et al*, 2000), see Materials and Methods) from single cell tracks of Venus::HES5 expression in spinal cord tissue ex-vivo (Manning et al. 2019). A KOP of 1 represents perfectly in phase synchronisation and 0 corresponds to no synchrony between single cells over time. We found that the KOP was between 0.15 and 0.4 (mean 0.3) (**Supp. Fig. 5b)**, which further reduced the parameter space of repression threshold and inter-cellular time delay that could fit the observed data (**Figure 5e,f**). The accepted parameter values for inter-cellular time delay were consistent with a Delta to HES5 transmission time of 128 min measured experimentally (Isomura *et al*, 2017). A Hill coefficient value larger than 2 was required for notable population dynamics to emerge (KOP>0) and only minor differences in terms of parameter selection were observed for values between 3 and 6 (**Supp. Fig 5c**).

This parameter exploration allowed us to optimise the search for spatial patterns that emerge at different coupling strengths using kymograph analysis (**Figure 5fg,h**). We set the inter-cellular time delay to 150 min and Hill Coefficient to 4 (Methods) and then compared the synthetic HES5 spatiotemporal characteristics at specific coupling strength levels (parameter space indicated by the white box in **Figure 5e**). Our comparison showed that strong coupling (i.e. high coupling strength or low inter-cellular repression threshold) induces *Salt and Pepper* dynamics whereby single neighbouring cells adopt either high oscillatory HES5 or stable low HES5 in an alternating spatial pattern that does not evolve over time (**Figure 5g**, *Salt and Pepper*, **Supp. Movie 2 first panel**). Meanwhile at mid-level coupling, the multiscale model induces globally synchronised oscillations in all cells (**Figure 5g,** *Global in phase* and **Supp. Movie 2 second panel**). At weak coupling strength, the spatial patterns show areas of local synchronisation emerging between neighbouring cells (**Figure 5g,** *Local in phase* and **Supp. Movie 2 third panel**). Under no coupling conditions we observed autonomous non-synchronised stochastic oscillations across the tissue (**Figure 5h** and **Supp. Movie 2 fourth panel**). These observed changes in synchronisation are indicated by population KOP values (**Figure 5g**) and we further confirmed that the KOPs correspond to changes in synchrony in terms of single cell expression dynamics between neighbouring cells (**Figure 5i**). As expected, in the uncoupled cells we observed no synchrony (KOP≈0) and random phase relationship between neighbouring cells (**Figure 5h,j**).

Our explorations of synthetic data show that at weak coupling strength microclusters can be generated in the model with a diameter of 2-6 cells (**Supp. Figure 5d**), consistent with cluster size in spinal cord tissue. However, the occurrence rate of microclusters was low, as these were observed around 20-30% of the time, although still higher than in the uncoupled situation (**Supp. Fig 5e** and **Supp. Fig 6a**). Thus, weak coupling conditions generate microclusters by promoting in-phase activity between neighbouring cells, however these

appear transiently and with low probability. In addition, the microclusters of locally synchronised cells were not spatially periodic (**Supp. Fig 5f**). As expected, at high coupling (low repression threshold) we detected an alternating pattern of HES5 with a spatial periodicity of 2 cells, which is a characteristic of Salt and Pepper (**Supp. Fig. 5f** and **Supp. Fig. 6b**).

In conclusion, our multicellular coupled model shows that spinal cord progenitors can locally synchronise at weak coupling strength to generate the microclusters of 2 to 6 cells seen in tissue, (**Figure 1d**) with single cell Venus::HES5 expression dynamics consistent with previous reports (Manning *et al.*, 2019). However, the model cannot recapitulate the repeated spatial co-ordination and continuous presence of dynamic microclusters, suggesting that additional mechanisms may act in the tissue environment to stabilise their presence and promote spatially periodic emergence.

The model predicts that probability of differentiation is regulated by the coupling strength between cells

To understand how the spatial pattern of HES5 and dynamic micropatterns in particular may affect properties of neurogenesis, we made the assumption that when HES5 is low, there is increased probability that the cell would differentiate consistent with findings that differentiation is accompanied by switching off of HES5, a repressor of neurogenesis (Bansod *et al.*, 2017; Manning *et al.*, 2019; Sagner *et al.*, 2018). We introduced a "differentiation threshold", which was set at the level of the HES5 population mean for each simulation (**Figure 5i,** *Population Mean***)** and we reasoned that if expression level in a cell dropped below this threshold there was an increasing probability to switch off HES5 and differentiate (**Figure 6a**).

We found that at high coupling strength (*Salt and Pepper* conditions) the probability to differentiate is the highest, whereas medium and weak coupling strength (corresponding to *Global* and *Local in phase* synchronisation, respectively) had progressively lower probability of differentiation (**Figure 6b)**. A similar trend was observed for the Coefficient of Variation (CoV, **Figure 6c**), a measure of variability denoting standard deviation over the mean. We investigated both the temporal (Temporal CoV) and spatial variation (Spatial CoV) in simulated HES5 expression (**Figure 6c**). Indeed, both temporal (indicative of single cell amplitude) and spatial CoV (indicative of variation between HES5 high and low regions in space) appear highest in *Salt and Pepper* conditions and lowest for *Local in phase* micropatterns (**Figure 6c**). However, we found that changes in spatial CoV correlated better with changes in rate of differentiation, especially at low repression threshold/high

coupling strength (**Figure 6c** versus **Figure 6b** *Salt and Pepper*). Thus, the strength of cell-to-cell coupling may influence the probability of differentiation through amplitude modulation by affecting how far the cells dip below the threshold of differentiation.

In tissue, HES5 spatial pattern varies predictably with the rate of differentiation

To test the computational prediction that the spatial pattern of HES5 (determined by the coupling strength) regulates the probability of differentiation, we compared the pattern in motorneuron and interneuron progenitor domains. We chose this comparison because at E10.5 the motorneuron domain is known to have a higher differentiation rate than the interneuron domain (Kicheva *et al*, 2014). We stained for the motorneuron progenitor marker OLIG2 (**Figure 7a** and **Supp. Fig. 7a**) and analysed expression levels of Venus::HES5 and Neurogenin 2 (NGN2) in the two domains. The motorneuron domain had lower HES5 levels and higher NGN2 levels than the interneuron domain consistent with the opposing activity of these genes on cell differentiation (Imayoshi & Kageyama, 2014).

We then used nuclear segmentation and pseudo-color analysis of mean Venus::HES5 intensity per nucleus (**Figure 7c**) and found that the interneuron domain shows the presence of microclusters mainly consisting of 2-3 cells wide in the dorsal to ventral axis whereas in the motoneuron domain high Venus::HES5 cells were mainly found as single cells, alternating with cells expressing lower Venus::HES5 (**Figure 7d**). We validated this finding further by investigating spatial periodicity by domain in live tissue slices. The domain border between motorneuron and interneuron progenitors was 35 μm ventral to the peak of HES5 expression (**Supp. Figure 7a,b**) allowing us to correctly identify the two domains without the need for an OLIG2 reporter in the same tissue (**Supp. Figure 7c-f**). We found that spatial periodicity was reduced in the motorneuron compared to the interneuron domain when analysed using both peak to peak distance in auto-correlation (**Figure 7e**, MN mean 31μm vs IN mean 41 μm and **Supp. Figure 7e**) and dominant spatial period by Lomb-Scargle periodogram (**Supp. Fig. 7f,** MN mean 25 μm vs IN mean 40 μm). Thus, both nuclear segmentation analysis and spatial periodicity indicated that, in the interneuron domain, microclusters of 2-3 cells are found in a spatially periodic pattern repeated every 4 cells. Meanwhile, the motorneuron domain shows alternating high and low HES5 levels between neighbouring cells and a significant reduction in spatial periodicity, both of which are pointing to the motorneuron domain more closely resembling *Salt and Pepper* conditions. Furthermore, we quantified differences in spatial peak to trough Venus::HES5 ratio between the two domains and found that spatial peak to trough amplitude is significantly increased in the motorneuron compared to interneuron domain (**Figure 7f**). This is consistent with our

model prediction that the spatial variation would appear significantly increased at high coupling corresponding to *Salt and Pepper* (**Figure 6c**).

Taken together, these results show that interneuron progenitors are more likely to be found in a locally synchronised state correlating with a lower rate of differentiation compared to progenitors in the motorneuron domain which are mostly found in alternating high-low (Salt and Pepper) pattern and show a higher rate of differentiation, as predicted computationally.

Discussion

In this paper, we have addressed the fine-grained pattern of neurogenesis in the spinal cord. How do cells co-ordinate their decisions with that of their neighbours so that neurogenesis takes place at a pace appropriate for the anatomical location? We have provided by monitoring the spatiotemporal patterning of key progenitor TF HES5 using live imaging analysis that is optimised towards revealing coordinated tissue level behaviour that would not be evident otherwise. In combination with computational modelling it enabled a multi-scale synthesis of the data with predictive power. We have uncovered an unexpected 3-tiered spatial and temporal organisation, which we discuss below in an ascending order of complexity.

First, within the ventral HES5 expression domain, which encompasses distinct MN and IN domains, we have discovered clusters of cells with positively corelated HES5 expression levels. These clusters, described for the first time here, are a maximum of 2-3 cells wide in D-V and 3-4 cells wide in A-B axes, hence termed microclusters. To detect microclusters, we removed longer range spatial trends such as overall gradients of intensity in HES5 expression (which have not been dealt further here) allowing us to concentrate on local correlations of expression. By following the HES5 in sparse individual cells in the same domain of expression, we have previously found oscillatory HES5 expression within the progenitor population (Manning *et al.*, 2019). The positively corelated microclusters described here, suggest that neighbouring cells are locally synchronised (in-phase) in HES5 expression a finding that was surprising because previous studies have suggested that in neurogenesis HES and DLL1 oscillators are in anti-phase in neighbouring cells (Kageyama *et al*, 2008; Shimojo *et al.*, 2016; Shimojo & Kageyama, 2016). DLL1 oscillations were observed with live imaging in tissue but only 2 neighbouring cells were monitored in close vicinity and a single example shown for anti-phase oscillations, which may explain the contradictions with our data. Thus, the discrepancy could be to a difference in scale of analysis or perhaps to the different molecules studied.

Second, we have found that HES5 microclusters are arrayed in a spatially periodic pattern along the D-V axis of the ventral HES5 domain, meaning that high and low HES5 expression clusters alternate regularly in space. Multiple stripes of Notch ligands DLL1 and JAG1 and Fringe proteins have been observed (Marklund *et al*, 2010; Ramos *et al*, 2010) but have not been analysed by an auto-correlation function thus, it is not known whether they occur on the same spatial scale as HES5. Such spatial periodicity at a fine level within the ventral HES5 domain contrasts with the large-scale organisation of HES5 in 2 separate broad domains along the D-V axis (Sagner *et al.*, 2018).

Thirdly, the HES5 spatial pattern of microclusters was not static but appeared dynamic over time; High HES5 expressing microclusters persisted for 6-8 hrs and then switched to low expression, while low expressing microclusters showed the opposite behaviour. In other words, high and low expressing microclusters alternated and sometimes created phase waves that travelled through the tissue over time. These waves are somewhat reminiscent of phase waves of LFNG and AXIN2 expression that are observed in somitogenesis (Baron & Galla, 2019; Sonnen *et al*, 2018; Tsiairis & Aulehla, 2016) however, in the spinal cord such phase waves were weak.

This complex spatial and temporal dynamic pattern of HES5 in spinal cord generated two important questions: how might it be generated and what might it mean for neurogenesis? Knowing that Hes genes and HES5 in particular, are activated by Notch signalling, we treated ex-vivo spinal cord tissue with DBZ to disrupt Notch signalling. We observed that the Notch inhibitor treatment extinguished spatial periodicity gradually and slowly, over a period of 12hrs, concurrent with HES5 level downregulation. This is consistent with the amplitude death that we observed in single cell data under the same treatment (Manning *et al.*, 2019). The effect of Notch inhibition was far more pronounced in the temporal nature of the pattern; in the absence of Notch signalling, the HES5 spatially periodic pattern of low and high expressing microclusters became “frozen” in time. These findings suggest that Notch signalling plays a part in making the pattern dynamic over time but cannot account for the entire spatiotemporal complexity of HES5 expression that we see ex vivo.

Computational modelling helped us to explore further the role of Notch in generating the spatiotemporal pattern of HES5 expression. We have used a simplified multiscale stochastic model of HES5 self-repression and inter-cellular coupling with delay, parameterised on our own experimental data, namely the single cell HES5 temporal period and extent of HES5 expression synchronicity between cells using the KOP. With this model we were able to explore the influence of the coupling strength between cells in producing spatiotemporal HES5 expression patterns. We found multiple spatiotemporal patterns, namely; a checkerboard-like Salt and Pepper patterning (at high coupling strength), global tissue synchronisation (at mid coupling strength), and random pattern (at no coupling), see **Supplem. Movie S2**. Importantly, at weak coupling strength and intercellular time delay that is consistent with previous reports, we observed the emergence of dynamic microclusters that matched our experimental observations. The emergence of dynamic patterns that do not resolve into steady HES “on” or “off”, rather than static patterns has been previously observed in a stochastic multicellular tissue model combining Notch-Delta and Hes auto-repression but not confirmed in tissue (Tiedemann *et al*, 2017). However, the dynamic microclusters in our model occurred infrequently (with a probability of 20-30%) even though

the model takes into consideration stochasticity and time delays; two features that represent well the tissue context. The low frequency of clusters did not improve after detailed optimised exploration of parameter space, which led us to conclude that a Notch based cell-to-cell signalling with the assumptions we have made, recapitulates only part of the observed pattern in vivo. Indeed, we note that a partial dependence of the spatiotemporally complex dynamic HES5 pattern is consistent with the ex-vivo Notch inhibition experiments. Extension of the model to include i) longer range cell-cell interaction via cytonemes, or due to the elongated shape of the progenitor cells, ii) increased complexity of the gene network such as cis-inhibition between Delta-Notch or differences in signalling between different Notch ligands, may be able to increase the fidelity of microcluster emergence. Indeed, it has been shown that such modifications increase the range of spatial patterns that can be obtained (Boareto *et al*, 2015; Cohen *et al.*, 2010; De Joussineau *et al*, 2003; Hadjivasiliou *et al*, 2019; Petrovic *et al*, 2014; Sprinzak *et al*, 2010). Other ways in which the model can be extended is to incorporate morphogen signalling gradients along the D-V axis or differentiation gradients along the A-B axis.

Nevertheless, the computational model we developed, allowed us to explore the advantages that organisation in dynamic microclusters may offer as a developmental strategy for neurogenesis in the embryonic spinal cord. Overall, we found that the spatiotemporal HES5 pattern was affected by the coupling strength between cells and in turn, affected the rate of differentiation. Based on our findings we propose that a classic lateral inhibition salt-and-pepper HES5 pattern (achieved at high coupling strength) shows the highest rate of differentiation because it generates two HES5 states ("on" and "off") in a spatially-alternating pattern with no further switching between the two. Global synchronisation (medium coupling strength) shows a medium rate of differentiation; however this regime is not observed in spinal cord data perhaps because the synchronous differentiation in "blocks" of tissue, although an appropriate developmental strategy for somitogenesis, may be incompatible with the structural integrity of the neural tissue or the finer diversification of neuronal fates within each domain. Random pattern (no coupling between cells) has similar rates of differentiation as weak coupling, however, weak coupling strength is advantageous because it allows local in phase synchronisation, which by analogy to global synchronisation (**Figure 6c**, *Global vs Local in phase)*, appears to transiently increase the amplitude of temporal oscillations in HES5 expression *(***Figure 5i***, panel 3-Local in phase*). This is important because a transient amplitude increase (due to the presence of microclusters at *Local in phase* conditions) could enable the ability of a cell to progress to differentiation. Indeed, we have previously shown that HES5 oscillations in proliferating spinal cord progenitors have low amplitude and show mainly aperiodic fluctuations (noisy dynamics) but the propensity to

oscillate as well as the peak-to-trough amplitude increases as cells enter the differentiation pathway (Manning *et al.*, 2019). We have also shown that when the transition from noisy dynamic expression to oscillatory expression does not take place, progenitor cells are unable to downregulate HES levels and differentiate (Soto *et al.*, 2020). We speculate that microclusters may act to select cells for differentiation by a transient increase in oscillation amplitude and the spatial periodicity of microclusters may space out differentiating cells to maintain tissue organisation.

We tested the hypothesis that by changing the HES5 spatiotemporal pattern through tuning the coupling strength, the tissue is able to fine tune the rate of neurogenesis. We compared the motorneuron and interneuron progenitor domains as these two neighbouring domains in the D-V axis are known to have different rates of differentiation (Kicheva *et al.*, 2014; Kuzmicz-Kowalska & Kicheva, 2020). Indeed, we find that that in the MN domain where the rate of differentiation is highest at E10.5, the HES5 pattern most closely matches the salt-and-pepper pattern **(Figure 8, MN)**. In the ventral interneuron domain, we propose that the local in phase synchronisation pattern (predicted to occur at weak coupling strength) is the closest match to the ex vivo situation **(Figure 8, IN)**. We propose it represents a strategy to balance prolonged neurogenesis, with a reasonable rate of differentiation and a transient increase in oscillation amplitude that is suitable for decoding by downstream genes. This supports our hypothesis that the spatial pattern relates to the rate of neurogenesis.

In conclusion, our findings show HES5 periodic micro-patterns exist in the developing spinal cord, they underlie the rate of neurogenesis and are an emergent property of the multi-scale synthesis of dynamical gene expression and Notch coupling. This temporally dynamic expression is a testament to the power of live tissue imaging in providing mechanistic insights of complex phenomena as they unfold in real time.

Materials and Methods

Animal experiments were performed by personal license holders under UK Home Office project license PPL70/8858 and within the conditions of the Animal (Scientific Procedures) Act 1986. Venus::HES5 knock-in mice (ICR.Cg-Hes5<tm1(venus)Imayo>) were obtained from Riken Biological Resource Centre, Japan and maintained as a homozygous line. In these mice the mVenus fluorescent protein is fused to the N-terminus of endogenous HES5. Sox1Cre:ERT2 mice (Sox1tm3(cre/ERT2)Vep were obtained from James Briscoe with the permission of Robin Lovell-Badge. R26R-H2B::mCherry mice were obtained as frozen

embryos from Riken Centre for Life Science Technologies, Japan and C57Bl6 mice were used as surrogates.

Embryo slicing and live imaging

Homozygous Venus::HES5 and either R26R-H2B::mCherry Sox1Cre:ERT2 or CD-1 mice were mated and E0.5 was considered as midday on the day a plug was detected. For matings with R26R-H2B::mCherry Sox1Cre:ERT2, intra-peritoneal injection of pregnant females with 2.5 mg Tamoxifen (Sigma) was performed 18 hours prior to embryo dissection. This enables single cell tracking through mosaic labelling of nuclei with H2B::mCherry. Whole embryos were screened for H2B::mCherry expression using Fluar 10x/0.5 objective on a Zeiss LSM880 confocal microscope. After decapitation, embryo bodies were embedded in 4% low-gelling temperature agarose (Sigma) containing 5mg/ml glucose (Sigma). 200µm transverse slices of the trunk containing the spinal cord around the forelimb region were obtained with the Leica VT1000S vibratome and released from the agarose. Embryo and slice manipulation were performed in phenol-red free L-15 media (ThermoFisher Scientific) on ice and the vibratome slicing was performed in chilled 1xPBS (ThermoFisher Scientific).

For snapshot imaging of live E10.5 spinal cord, slices were stained with 50µM Draq5 (Abcam – ab108410) in 1xPBS (ThermoFisher Scientific) for 1.5hrs on ice if required, and then placed directly on to a 35mm glass-bottomed dish (Greiner BioOne). Images were acquired with a Zeiss LSM880 microscope and C-Apochromat 40x 1.2 NA water objective. E10.5 spinal cord slices for live timelapse microscopy were placed on a 12mm Millicell cell culture insert (MerckMillipore) in a 35mm glass-bottomed dish (Greiner BioOne) incubated at 37°C and 5%CO_2. The legs of the cell culture insert were sanded down to decrease the distance from the glass to the tissue. 1.5mls of DMEM F-12 (ThermoFisher Scientific) media containing 4.5mg/ml glucose, 1x MEM non-essential amino acids (ThermoFisher Scientific), 120ug/ml Bovine Album Fraction V (ThermoFisher Scientific), 55µM 2-mercaptoethanol, 1x GlutaMAX (ThermoFisher Scientific), 0.5x B27 and 0.5x N2 was added. Movies were acquired using Zeiss LSM880 microscope and GaAsP detectors. A Plan-Apochromat 20x 0.8 NA objective with a pinhole of 5AU was used. 10 z-sections with 7.5 µm interval were acquired every 15 mins for 18-24 hrs. DMSO (Sigma) or 2µM DBZ (Tocris) was added to media immediately before imaging.

Microcluster quantification and correlation of nuclear Venus::HES5 intensity with distance and neighbours

Individual Draq5+ nuclei were manually segmented as ellipses using ImageJ, converted to a mask and subsequently eroded using the ImageJ function ‘erode’ to ensure no overlap between nuclei. Small nuclei with very high Draq5 intensity were removed to avoid dead or dying cells. The mean intensity of each nuclear ROI was plotted using the ‘viridis’ LUT. Microcluster size was calculated by quantile normalising the distribution of Venus::HES5 intensities across experiments, then counting the maximum number of adjacent cells in the highest colour band of the viridis LUT. The centroids of the manually segmented cells were used to measure distance and hence rank between neighbours and a correlation of the distance and mean nuclear Venus::HES5 intensity was calculated using the ‘corr’ function in MATLAB. Mean nuclear Venus::HES5 intensity was also randomised between nuclei and repeated 100 times before undergoing the same distance vs mean intensity correlation.

Centre of intensity detection and radial gradient analysis

The centre of intensity (COI) was calculated using a centre of mass approach. The intensity of each nuclei was multiplied by their position. These were then summed and divided by the sum of all nuclear intensities. The COI was used to sort cells in to 5 equally spaced radial zones with increasing distance from the COI. The mean Venus::HES5 intensity of nuclei in these zones was calculated and then subtracted from each nucleus in that zone to remove the radial gradient. A simulated radial gradient from a single focal point in the image was generated using

$$I_r = Z + \alpha x_r$$

Where $\mathbf{I_r}$ is the new intensity of the cells, Z is simulated intensities with the mean and variance similar to that of real data, α is the gradient strength parameter and x_r is a function of the distance from the centre of intensity**.** As α increases the radial gradient is less affected by random deviation in HES5 expression.

Detection and periodicity analysis of spatial periodic HES5 patterns

Movies were first subject to image registration in Imaris (Bitplane) by tracking an invariant part of the tissue. Bleach correction was then performed using a ratiometric method in ImageJ. Spatial expression profiles and kymographs were generated in Zen Blue (Carl Zeiss Microscopy) by drawing a spline 15 µm wide starting ventrally and extending parallel to the ventricle in the dorsal direction, then using the ‘Line profile’ or ‘Kymograph’ function. A 15 µm width was chosen as this covered more than a cell width and the average distance a cell

travels in 2-2.5 hrs, the value used for time averaging. 0 distance corresponded to the ventral most end of the spline. Apical, medium and basal expression profiles and kymographs were generated from splines around 10, 30 and 60 µm from the ventricle respectively, and analysing each side of the ventricle separately. 2-3 non-overlapping z-sections were used to generate kymographs per movie. Expression profile data for Draq5 from single snapshot images of live slices was generated in ImageJ using a rectangular ROI of width 15µm and the "Plot profile" function.

Kymographs were analysed using custom scripts in MATLAB. Kymographs were averaged along the time axis in 2-2.5 hr windows. Subsequently spatial Venus::HES5 intensity in the ventral-dorsal direction was de-trended by fitting a polynomial and subtracting this from the raw data. This removed the larger trend due to the profile of the HES5 expression domain.

Auto-correlation and Lomb-Scargle periodograms were used to analyse periodicity of the de-trended spatial intensity plots. Lomb-Scargle periodograms were generated with the MATLAB 'plomb' function and plotting power level thresholds as specified in figure legends. Auto-correlation was performed with the MATLAB 'xcorr' function. Auto-correlation functions were smoothed using Savitzky-Golay filter and then peaks identified using the 'find peaks' function. Significant peaks were identified using a bootstrap method with 100 randomisations. Auto-correlations were randomised and then re-subjected to auto-correlation. 2 standard deviations of the auto-correlations of randomised data was used as a threshold and peaks were designated as significant if they exceeded this threshold. The mean distance between significant peaks was calculated per kymograph timepoint. Fold-changes of spatial intensities were calculated between significant peaks and troughs in the signal identified using 'find peaks' on the negative signal.

Splitting Venus::HES5 kymographs in to motorneuron and interneuron domains was based on staining of cryo-sectioned E10.5 spinal cord with motorneuron progenitor domain marker OLIG2. The peak of the trend in Venus::HES5 was found to occur on average at 35 µm dorsally from the edge of the OLIG2+ domain. This criteria was used to split kymographs from movies of Venus::HES5 spinal cords that had not been immuno-stained.

Hierarchical clustering of local HES5 expression and microcluster persistence time

Kymographs of HES5 expression were split into adjacent 20µm regions along the D-V axis and the HES5 intensity averaged in these regions to give a timeseries per region. These timeseries were normalized to the mean and standard deviation of each region over time (z-scoring) and subject to hierarchical clustering using the *clustergram,m* routine in MatLab with

euclidean distance and average linkage. The persistence time was calculated as continuous time when the signal in the region was above (high) or below (low) its mean level. The persistence ratio was calculated as the time interval spent in a high state divided by the time interval spent in a low state within the same 20µm region. Where only high or low persistence time intervals were detected in a region these observations were excluded from the ratio. For the calculation of phase synchronisation index see **Spatial phase synchronisation**.

Single cell tracking over time

Single neural progenitor cells in E10.5 spinal cord slices were tracked in Imaris on the H2BmCherry channel using the 'Spots' function with background subtraction and the Brownian motion algorithm. All tracks were manually curated to ensure accurate single-cell tracking. Background fluorescence was measured via an ROI drawn on a non-Venus::HES5 expressing region on the tissue and subtracted from spot intensity. To account for any photobleaching and allow comparison of intensities between movies the mean intensity of mCherry and Venus in each spot was normalised to the mean intensity of mCherry or Venus in the whole tissue. The whole tissue volume was tracked using the 'Surfaces' and 'Track over time' function. For the calculation of Kuramoto order parameter from timeseries (**Figure 5b**) see **Temporal phase synchronisation**.

Immunofluorescent staining

Trunks of E10.5 embryos for cryo-sectioning were fixed in 4% PFA for 1 hour at 4°C, followed by 3 quick washes with 1xPBS and 1 longer wash for 1 hour at 4°C. Embryos were equilibrated overnight in 30% sucrose (Sigma) at 4°C before mounting in Tissue-Tek OCT (Sakura) in cryomoulds and freezing at -80°C. 12µm sections were cut on Leica CM3050S cryostat. E10.5 spinal cord slices cultured on Millicell inserts were fixed in 4% PFA for 4 hours. For staining, tissue and sections were washed in PBS followed by permeabilisation in PBS 0.2% Triton X-100 (Sigma) and blocking with PBS 0.05% Tween20 (Sigma) + 5% BSA (Sigma). Primary and secondary antibodies were diluted in PBS 0.05% Tween20 + 5% BSA. Tissue was incubated with primary antibodies overnight at 4°C, then washed three times for 5–10 minutes in PBS 0.05% Tween20, incubated with secondary antibodies and DAPI (Sigma) for 6 hours at room temperature, and washed again three times in PBS-T. Sections were mounted using mowiol 4-88 (Sigma). Primary antibodies used were rabbit anti-SOX2

(ab97959, 1:200), rabbit anti-OLIG2 (EMD Millipore AB9610, 1:200) and goat anti-NGN2 (Santa Cruz Biotechnology sc-19233, 1:200).

Statistical testing

Statistical tests were performed in GraphPad Prism 8. Data was tested for normality with D'Agostino-Pearson test. The relevant parametric or non-parametric test was then performed. Bar plots and discrete scatter plots show mean mean±SD where multiple independent experiments are analysed. Statistical significance between 2 datasets was tested with either t-test (parametric) or Mann-Whitney test (non-parametric). Statistical significance ($p<0.05$) for 2+ datasets was tested by Kruskall-Wallis with Dunn's multiple comparison correction. All tests were 2-sided. Multiple comparison testing involved comparing all pairs of data columns. Correlations were analysed using Pearson correlation coefficient. Sample sizes, experiment numbers, p values<0.05 and correlation coefficients are reported in each figure legend.

Stochastic model of auto-repression coupled between cells

We adapted a HES5-parameterised single-cell model from previous work into a Notch-Delta-coupled multicellular model (**Figure 5a**) (Manning *et al.*, 2019). The single cell network is the basic unit of the model and consists of negative feedback loop of HES5 protein onto its own mRNA expression described by stochastic delay differential equations (SDDEs) capable of producing stochastic autonomous oscillations. The SDDEs implement a Langevin approach over a Gillespie algorithm in favour of reduced computational cost and fixed time steps which enable easier addition of time delays (Gillespie, 2000).

To extend the single cell model to a multicellular one, the cells were coupled together with an interaction representative of the Notch-Delta pathway and its interaction with HES5. Instead of modelling every reaction in the chain of events that constitute the Notch-Delta pathway, we used a highly adjustable coupling function – an inhibitory Hill function – that requires only two parameters to specify its shape. This drastically reduced the potential number of parameters required to describe the Notch-Delta pathway that couples HES5 dynamics between cells while maintaining the ability to describe a wide variety of possible coupling function shapes that may represent the biological system. The Hill function in this model therefore describes how the production rate of HES5 in one cell is inhibited by high levels of HES5 expression in a neighbouring cell and has the form of

$$J(P) = \frac{1}{1 + \left(\frac{P}{P_0}\right)^n} \tag{1}$$

where $J(P)$is the mRNA production rate response of a cell to the concentration of protein P in a neighbouring cell, P_0 is the repression threshold (also known as the effective concentration EC50) and n is the Hill coefficient. P_0 and n define the shape of the Hill function (illustrated in **Figure 5b**) and thus how a cell will respond to the levels of HES5 in its neighbouring cells. Specifically, we refer to repression threshold as the inverse of the coupling strength as this parameter defines at what concentrations of HES5 in a neighbouring cell a receiving cell becomes repressed. The Hill coefficient is also capable of changing the coupling strength but to a lesser extent as it affects the slope of the curve around the value of the repression threshold, creating a more step-like response at high Hill coefficient value and reproducing a Michaelis-Menten curve at a value of 1.

For the analysis in this paper, we chose neighbours to be taken as the closest or first rank neighbours, which in the case of hexagonal geometry implies a cell can be coupled to the dynamics of a maximum of 6 immediate neighbours (illustrated in **Figure 5c**). The incoming protein concentration that a cell experiences is defined as the average of its neighbours

$$\bar{P} = \frac{1}{N}\sum_{n=1}^{N} P_n \tag{2}$$

where N is the number of neighbouring cells and P_n is the protein concentration in neighbouring cell n. Equation (2) assumes that a cell receives equal contribution from each of its neighbouring cells, and there is no efficiency of signalling or scaling parameter in (2) as this would be redundant in addition to the intercellular repression threshold. Taking into account the number of neighbours ($\frac{1}{N}$ in (2)) rather than a static multiplication term reduces the effects of different patterning at the boundaries of the simulated tissue and was found to result in similar dynamics as when periodic boundaries were used.

Finally, to capture the dynamics of the Notch-Delta pathway more accurately, a time delay was added to the Hill function. The use of a nonlinear function to describe the multiple steps neglects the time-delays associated with the reaction, transport/diffusion, and synthesis, so an explicit time delay parameter was added. The full form of the coupling function taking into account the neighbours and time delay is given by

$$J\left(\bar{P}(t - \tau_{ND})\right) = \frac{1}{1 + \left(\frac{\bar{P}(t - \tau_{ND})}{P_{ND0}}\right)^{n_{ND}}} \tag{3}$$

where the subscript ND indicates intercellular parameters associated with Notch-Delta signalling and τ_{ND} is the intercellular time delay.

The full set of equations that describe the dynamics in an individual cell within the multicellular model is the single cell model from previous work (Manning *et al.*, 2019) but with the introduction of (3) as a multiplicative term that affects the production rate of mRNA

$$\frac{dM(t)}{dt} = -\mu_m M(t) + \alpha_m G\big(P(t-\tau_H)\big) J\big(\bar{P}(t-\tau_{ND})\big) + \sqrt{\mu_m M(t) + \alpha_m G\big(P(t-\tau_H)\big) J\big(\bar{P}(t-\tau_{ND})\big)}\,\xi_m(t) \tag{4}$$

$$\frac{dP(t)}{dt} = -\mu_p(t) P(t) + \alpha_p M(t) + \sqrt{\mu_p(t) P(t) + \alpha_p M(t)}\,\xi_p(t) \tag{5}$$

Where M is HES5 mRNA concentration, $\mu_{m,p}$ are the degradation rate of HES5 mRNA and protein respectively, $\alpha_{m,p}$ are the transcription and translation rates of HES5, $\xi_{m,p}$ are Gaussian white noise, and $G\big(P(t-\tau_H)\big)$ is an inhibitory Hill function that describes Hes5 autorepression

$$G\big(P(t-\tau_H)\big) = \frac{1}{1 + \left(\frac{P(t-\tau_H)}{P_{H0}}\right)^{n_H}} \tag{6}$$

where P_{H0} is the repression threshold for HES5 acting on its own promoter and n_H is the corresponding Hill coefficient. The multiplicative nature of the two Hill functions in (4) is based on previous literature (Chikayama, 2014; Lewis, 2003)

In (4) and (5), there is a deterministic part which represents the overall increase or decrease in protein or mRNA to be expected at given concentrations and then a stochastic part that accounts for random binding or non-binding of transcription and translation machinery in the cell. The stochastic part is scaled by the square root of the number of events that can happen in a given time and so the stochastic part becomes increasingly significant at low protein/mRNA numbers. The Euler–Maruyama method was used to numerically calculate solutions to the SDDEs in (4) and (5) using a time step size of 1 minute.

Parameter values for simulations of the model included in **Figure 5** and **Supp. Figure 5** are given in **Supp. Table 1 Main**. We also investigated several other parameter combinations (**Supp. Table 1** C15/10/5-1 to 3 and **Supp. Figure 6**) previously identified to reproduce HES5 tissue data by Bayesian inference (Manning *et al.*, 2019).

Synthetic kymograph and spatial data generation

The 15µm strips used for spatial analysis in the experimental data (**Figure 2a**) were found to correspond to a width of 1-2 nuclei. Therefore, to obtain similar data from the model, spatial

signals were generated by averaging 2 adjacent columns of cells. This single column of averaged data was used for generating each time point in the kymographs (**Figure 5g,h**) and also to test cluster occurrence and spatial periodicity (**Supp. Fig 5e,f** and **Supp. Fig 6a,b**).

Parameter space explorations and parameter selection

Parameter space 2D maps were used to visualise regions of different model behaviour (**Figure 5d-f**, **Supp. Figure 5c,e,f**, and **Supp. Figure 6a,b**). These parameter spaces have intercellular time delay plotted along x-axis and repression threshold value along the y-axis and at each point an output value of the model is plotted (e.g. temporal period). For each grid point in parameter space, the average output from 5 simulations with random initial conditions is shown. Parameter selection **(Figure 5f)** was used to identify suitable ranges for intercellular time delay and repression threshold by comparing statistics from synthetic data against experimental statistics obtained from tissue data whereby synthetic data values found within 2.4 standard deviations away from the experimental mean were accepted. Parameter selection was performed separately for temporal period and Kuramoto order parameter (see **Phase reconstruction**). Temporal period was computed from synthetic timeseries of HES5 as inverse of dominant frequency peak from power spectrum reconstruction by FFT. Temporal period used for parameter selection was average period per simulation where single cell period estimates above 10h were excluded as non-oscillatory.

Phase reconstruction and Kuramoto order value as a measure of synchrony

To determine the synchronisation of real signals both in the model and experimental data, the phase of each oscillator was first reconstructed in complex space. This reconstruction was achieved by using the Hilbert transform, which shifts the phase of each frequency component in a signal by 90 degrees (Benedetto, 1996). The Hilbert transform of a function $u(t)$ is defined as

$$H(u)(t) = \frac{1}{\pi} \int_{-\infty}^{\infty} \frac{u(\tau)}{t-\tau} d\tau. \qquad (7)$$

To obtain a rotating vector that contains both the amplitude and phase information of the signal at a given time t, the original signal and the 90 degrees shifted Hilbert transform can be combined in complex space to give

$$u_a(t) = u(t) + i \cdot H(u)(t). \quad (8)$$

By comparing $u_a(t)$ of two or more cells, a measure of how synchronised a population of cells is can be determined by first calculating what is known as the complex order parameter

$$\psi = \frac{1}{N}\sum_{j=1}^{N} e^{i\phi_j} \quad (9)$$

where N is the number of oscillators and ϕ_j is the phase of oscillator j. From this, the Kuramoto order parameter is defined as the absolute value of the complex order parameter ψ, which is the magnitude of the vector and has a value between 0 and 1 (Choi *et al.*, 2000). A value of 1 indicates perfect synchrony and matching phase, meaning that in complex space the phases of each oscillator would be at the same angle and would rotate at the same frequency. A value of 0 indicates no synchronisation, and in complex space would appear as a random distribution of phases that average to a point at the origin.

Spatial and temporal phase synchronisation

In addition to calculating KOPs, we also used the Hilbert transform to extract phase from spatial data to determine how dynamic the positions of peak and trough were over time. This involved extracting and plotting the phase from time-averaged spatial signals as shown in **Figure 3h** and **Figure 4f**. The phase synchronisation index for DMSO and DBZ conditions (**Figure 4g)** was obtained by calculating KOP per position in D-V axis and averaging per z-slice (with left and right of the ventricle analysed separately).

Synthetic microcluster occurrence and diameter calculation

To detect presence of clusters of similar expressing cells in the synthetic data, spatial kymograph data was first smoothed using a polynomial fit. At each time point, the maximal peak in the polynomial was identified, followed by identification of the nearest trough below 80% the value of the peak which is consistent with a 1.2x spatial fold change in amplitude. The presence of a peak and trough satisfying these conditions is indicative of a cluster at a specific timepoint. The frequency of cluster occurrence was calculated as the number of time points in a simulation a cluster was identified.

The microcluster diameter was calculated from spatial data by searching for groups of cells that exhibit local in-phase characteristics. We performed phase reconstruction followed by pairwise phase synchronisation measurements by KOP (see Phase reconstruction) and

counted the number of neighbouring cells in phase by filtering for KOPi,j >0.9 where I, j indicate neighbouring positions in the grid.

Rate of differentiation from synthetic data

We explored how absolute sensing of HES5 by downstream targets might affect the rate of differentiation at different intercellular repression thresholds (coupling strengths) by assuming a simple linear differentiation condition where lower HES5 levels increase the probability of a cell committing to eventual differentiation (**Figure 6a**). This assumption is based on the fact that HES5 represses downstream proneural targets which promote a cell to head towards a differentiated state.

Because the level of expression changes as the coupling strength is varied, no set absolute threshold is assumed, instead a differentiation threshold is determined from the mean population expression in each simulation. Above this threshold, a cell has a zero chance of differentiation, whereas below the threshold has a linearly increasing probability of differentiation the further it drops below the threshold. A probability is calculated at each time point with no memory of past HES5 dynamics and is calculated as

$$P_{diff} = \begin{cases} 0, & P(t) > D_{thresh} \\ R\left(\dfrac{D_{thresh} - P(t)}{D_{thresh}}\right), & P(t) < D_{thresh} \end{cases} \qquad (10)$$

where R is the differentiation rate (with units of Δt^{-1} as probability of differentiation is calculated on every time step), and D_{thresh} is the differentiation threshold.

Cells are simply marked as having differentiated in this setup, and the dynamics of an individual cell remain the same after a differentiation event, which can be thought of an asymmetric division, where the differentiating cell leaves the population and it's space in the grid is filled with a non-differentiating cell. Differentiation rate is calculated by taking the total number of differentiation events in a simulation and dividing by the total time. Single cell parameters used are shown in **Supp. Table 1**, and the multicellular parameters used were $n_{ND} = 4$, $\tau_{ND} = 150$ minutes, and range of repression thresholds were explored $500 < P_{ND0} < 30000$.

Code and Data availability

All code written in MatLab and is available from the authors upon request.

Acknowledgements

We are grateful to members of the Papalopulu lab, Andrew Hazel, James Briscoe and Andy Oates for advice and discussions. The authors would also like to thank the Biological Services Facility and the Bioimaging Facilities of the University of Manchester for technical support. CM was supported by a Sir Henry Wellcome Fellowship (103986/Z/14/Z) and University of Manchester Presidential Fellowship. VB was supported by a Wellcome Trust Senior Research Fellowship to NP (090868/Z/09/Z). JH, EJ and DH (Wellcome Trust Grant No. 215189/Z/19/Z) were supported by Wellcome Trust PhD studentships. JK was supported by Wellcome Trust Senior Research Fellowship to NP and a University of St Andrews Lectureship. The funders had no role in study design, data collection and analysis, decision to publish, or preparation of the manuscript.

Author Contributions

CM and NP conceived and designed the experimental study.

CM performed wet lab experiments, supervised and performed data analysis, interpreted data and wrote the paper.

VB supervised and performed development of method to analyse spatial micropatterns of HES5 expression both in data and from the model, developed method for Hilbert phase persistence analysis, performed data analysis, interpreted data and wrote the paper.

JH designed and implemented stochastic coupled HES5 model, explored parameterization, analysed and interpreted the model.

EJ collected data and developed method to analyse correlations of HES5 nuclear intensity.

DH contributed to the method to analyse periodic spatial micropatterns of HES5 expression.

JK supervised and assisted design, analysis and interpretation of the mathematical model.

PG supervised and assisted analysis and interpretation of the mathematical model.

NP supervised and directed the work, interpreted data and co-wrote the paper with CM, VB and JH with input from JK, EJ, DH and PG.

Competing Financial interests

None.

References

Bansod S, Kageyama R, Ohtsuka T (2017) Hes5 regulates the transition timing of neurogenesis and gliogenesis in mammalian neocortical development. *Development (Cambridge)* 144: 3156-3167

Baron JW, Galla T (2019) Intrinsic noise, Delta-Notch signalling and delayed reactions promote sustained, coherent, synchronized oscillations in the presomitic mesoderm. *J R Soc Interface* 16: 20190436

Benedetto JJ (1996) *Harmonic analysis and applications*. CRC Press

Boareto M, Jolly MK, Lu M, Onuchic JN, Clementi C, Ben-Jacob E (2015) Jagged-delta asymmetry in Notch signaling can give rise to a sender/receiver hybrid phenotype. *Proceedings of the National Academy of Sciences of the United States of America* 112: E402-E409

Bonev B, Stanley P, Papalopulu N (2012) MicroRNA-9 Modulates Hes1 ultradian oscillations by forming a double-negative feedback loop. *Cell Rep* 2: 10-18

Briscoe J, Small S, 2015. Morphogen rules: Design principles of gradient-mediated embryo patterning. Company of Biologists Ltd, pp. 3996-4009.

Chikayama RCEaE (2014) A Theory of Decomposition of Complex Chemical Networks using the Hill Functions

. *arXiv*: 1405.5621

Choi MY, Kim HJ, Kim D, Hong H (2000) Synchronization in a system of globally coupled oscillators with time delay. *Phys Rev E Stat Phys Plasmas Fluids Relat Interdiscip Topics* 61: 371-381

Cohen M, Georgiou M, Stevenson NL, Miodownik M, Baum B (2010) Dynamic Filopodia Transmit Intermittent Delta-Notch Signaling to Drive Pattern Refinement during Lateral Inhibition. *Developmental Cell*

Corson F, Couturier L, Rouault H, Mazouni K, Schweisguth F (2017) Self-organized Notch dynamics generate stereotyped sensory organ patterns in Drosophila. *Science (New York, NY)* 356: eaai7407-eaai7407

Das RM, Storey KG (2012) Mitotic spindle orientation can direct cell fate and bias Notch activity in chick neural tube. *EMBO Rep* 13: 448-454

Das RM, Storey KG (2014) Apical abscission alters cell polarity and dismantles the primary cilium during neurogenesis. *Science* 343: 200-204

De Joussineau C, Soulé J, Martin M, Anguille C, Montcourrier P, Alexandre D (2003) Delta-promoted filopodia mediate long-range lateral inhibition in Drosophila. *Nature* 426: 555-559

de Lichtenberg KH, Funa N, Nakic N, Ferrer J, Zhu Z, Huangfu D, Serup P (2018) Genome-Wide Identification of HES1 Target Genes Uncover Novel Roles for HES1 in Pancreatic Development. *bioRxiv*: 335869

Delile J, Rayon T, Melchionda M, Edwards A, Briscoe J, Sagner A (2019) Single cell transcriptomics reveals spatial and temporal dynamics of gene expression in the developing mouse spinal cord. *Development*: dev.173807-dev.173807

Galla T (2009) Intrinsic fluctuations in stochastic delay systems: Theoretical description and application to a simple model of gene regulation. *Physical Review E* 80: 021909-021909

Gillespie DT (2000) The chemical Langevin equation. *The Journal of Chemical Physics* 113: 297-306

Goodfellow M, Phillips NE, Manning C, Galla T, Papalopulu N (2014) microRNA input into a neural ultradian oscillator controls emergence and timing of alternative cell states. *Nat Commun* 5: 3399

Hadjivasiliou Z, Moore RE, McIntosh R, Galea GL, Clarke JDW, Alexandre P (2019) Basal Protrusions Mediate Spatiotemporal Patterns of Spinal Neuron Differentiation. *Developmental Cell* 49: 907-919.e910

Henrique D, Schweisguth F (2019) Mechanisms of Notch signaling: a simple logic deployed in time and space. *Development* 146

Herrgen L, Ares S, Morelli LG, Schröter C, Jülicher F, Oates AC (2010) Intercellular coupling regulates the period of the segmentation clock. *Current Biology* 20: 1244-1253

Hunter GL, Hadjivasiliou Z, Bonin H, He L, Perrimon N, Charras G, Baum B (2016) Coordinated control of Notch/Delta signalling and cell cycle progression drives lateral inhibition-mediated tissue patterning. *Development (Cambridge, England)* 143

Imayoshi I, Isomura A, Harima Y, Kawaguchi K, Kori H, Miyachi H, Fujiwara T, Ishidate F, Kageyama R (2013) Oscillatory control of factors determining multipotency and fate in mouse neural progenitors. *Science* 342: 1203-1208

Imayoshi I, Kageyama R (2014) bHLH factors in self-renewal, multipotency, and fate choice of neural progenitor cells. *Neuron* 82: 9-23

Isomura A, Ogushi F, Kori H, Kageyama R (2017) Optogenetic perturbation and bioluminescence imaging to analyze cell-to-cell transfer of oscillatory information. *Genes and Development* 31: 524-535

Jensen MH, Sneppen K, Tiana G (2003) Sustained oscillations and time delays in gene expression of protein Hes1. *FEBS Letters* 541: 176-177

Kageyama R, Ohtsuka T, Shimojo H, Imayoshi I (2008) Dynamic Notch signaling in neural progenitor cells and a revised view of lateral inhibition. *Nature Neuroscience* 11: 1247-1251

Kicheva A, Bollenbach T, Ribeiro A, Valle HP, Lovell-Badge R, Episkopou V, Briscoe J (2014) Coordination of progenitor specification and growth in mouse and chick spinal cord. *Science (New York, NY)* 345: 1254927-1254927

Kobayashi T, Mizuno H, Imayoshi I, Furusawa C, Shirahige K, Kageyama R (2009) The cyclic gene Hes1 contributes to diverse differentiation responses of embryonic stem cells. *Genes Dev* 23: 1870-1875

Kuzmicz-Kowalska K, Kicheva A (2020) Regulation of size and scale in vertebrate spinal cord development. *Wiley Interdiscip Rev Dev Biol*: e383

Lewis J (2003) Autoinhibition with transcriptional delay. *Current Biology* 13: 1398-1408

Ma Q, Chen Z, del Barco Barrantes I, de la Pompa JL, Anderson DJ (1998) neurogenin1 is essential for the determination of neuronal precursors for proximal cranial sensory ganglia. *Neuron* 20: 469-482

Manning CS, Biga V, Boyd J, Kursawe J, Ymisson B, Spiller DG, Sanderson CM, Galla T, Rattray M, Papalopulu N (2019) Quantitative single-cell live imaging links HES5 dynamics with cell-state and fate in murine neurogenesis. *Nature communications*

Marklund U, Hansson EM, Sundström E, de Angelis MH, Przemeck GK, Lendahl U, Muhr J, Ericson J (2010) Domain-specific control of neurogenesis achieved through patterned regulation of Notch ligand expression. *Development* 137: 437-445

Momiji H, Monk NAM (2008) Dissecting the dynamics of the Hes1 genetic oscillator. *Journal of Theoretical Biology* 254: 784-798

Monk NAM (2003) Oscillatory Expression of Hes1, p53, and NF-κB driven by transcriptional time delays. *Current Biology* 13: 1409-1413

Morelli LG, Ares S, Herrgen L, Schröter C, Jülicher F, Oates AC (2009) Delayed coupling theory of vertebrate segmentation. *HFSP Journal* 3: 55-66

Nelson BR, Hodge RD, Daza RA, Tripathi PP, Arnold SJ, Millen KJ, Hevner RF (2020) Intermediate progenitors support migration of neural stem cells into dentate gyrus outer neurogenic niches. *Elife* 9

Oates AC (2020) Waiting on the Fringe: cell autonomy and signaling delays in segmentation clocks. *Curr Opin Genet Dev* 63: 61-70

Ohtsuka T, Ishibashi M, Gradwohl G, Nakanishi S, Guillemot F, Kageyama R (1999) Hes1 and Hes5 as notch effectors in mammalian neuronal differentiation. *The EMBO journal* 18: 2196-2207

Özbudak EM, Lewis J (2008) Notch signalling synchronizes the zebrafish segmentation clock but is not needed to create somite boundaries. *PLoS Genetics* 4

Paridaen JT, Huttner WB (2014) Neurogenesis during development of the vertebrate central nervous system. *EMBO Rep* 15: 351-364

Petrovic J, Formosa-Jordan P, Luna-Escalante JC, Abello G, Iban M, Es, Neves J, Giraldez F, Abelló G, Ibañes M *et al* (2014) Ligand-dependent Notch signaling strength orchestrates lateral induction and lateral inhibition in the developing inner ear. *Development (Cambridge)* 141: 2313-2324

Phillips NE, Manning CS, Pettini T, Biga V, Marinopoulou E, Stanley P, Boyd J, Bagnall J, Paszek P, Spiller DG *et al* (2016) Stochasticity in the miR-9/Hes1 oscillatory network can account for clonal heterogeneity in the timing of differentiation. *Elife* 5

Ramos C, Rocha S, Gaspar C, Henrique D (2010) Two Notch ligands, Dll1 and Jag1, are differently restricted in their range of action to control neurogenesis in the mammalian spinal cord. *PLoS One* 5: e15515

Sagner A, Briscoe J, 2019. Establishing neuronal diversity in the spinal cord: A time and a place. Company of Biologists Ltd.

Sagner A, Gaber ZB, Delile J, Kong JH, Rousso DL, Pearson CA, Weicksel SE, Melchionda M, Mousavy Gharavy SN, Briscoe J *et al* (2018) Olig2 and Hes regulatory dynamics during motor neuron differentiation revealed by single cell transcriptomics. *PLOS Biology* 16: e2003127-e2003127

Shaya O, Sprinzak D, 2011. From Notch signaling to fine-grained patterning: Modeling meets experiments. pp. 732-739.

Shimojo H, Isomura A, Ohtsuka T, Kori H, Miyachi H, Kageyama R (2016) Oscillatory control of Delta-like1 in cell interactions regulates dynamic gene expression and tissue morphogenesis. *Genes & development* 30: 102-116

Shimojo H, Kageyama R, 2016. Oscillatory control of Delta-like1 in somitogenesis and neurogenesis: A unified model for different oscillatory dynamics. Academic Press, pp. 76-82.

Sonnen KF, Lauschke VM, Uraji J, Falk HJ, Petersen Y, Funk MC, Beaupeux M, François P, Merten CA, Aulehla A (2018) Modulation of Phase Shift between Wnt and Notch Signaling Oscillations Controls Mesoderm Segmentation. *Cell* 172: 1079-1090.e1012

Soto X, Biga V, Kursawe J, Lea R, Doostdar P, Thomas R, Papalopulu N (2020) Dynamic properties of noise and Her6 levels are optimized by miR-9, allowing the decoding of the Her6 oscillator. *The EMBO Journal*

Sprinzak D, Lakhanpal A, Lebon L, Santat LA, Fontes ME, Anderson GA, Garcia-Ojalvo J, Elowitz MB (2010) Cis-interactions between Notch and Delta generate mutually exclusive signalling states. *Nature* 465: 86-90

Tiedemann HB, Schneltzer E, Beckers J, Przemeck GKH, Hrabě de Angelis M (2017) Modeling coexistence of oscillation and Delta/Notch-mediated lateral inhibition in pancreas development and neurogenesis. *Journal of Theoretical Biology* 430: 32-44

Tsiairis CD, Aulehla A (2016) Self-Organization of Embryonic Genetic Oscillators into Spatiotemporal Wave Patterns. *Cell* 164: 656-667

Vilas-Boas F, Fior R, Swedlow JR, Storey KG, Henrique D (2011) A novel reporter of notch signalling indicates regulated and random Notch activation during vertebrate neurogenesis. *BMC Biol* 9: 58

Webb AB, Lengyel IM, Jörg DJ, Valentin G, Jülicher F, Morelli LG, Oates AC (2016) Persistence, period and precision of autonomous cellular oscillators from the zebrafish segmentation clock. *eLife* 5

Figure Legends

Figure 1. Microclusters of spinal cord neural progenitor cells have positively correlated HES5 levels.

(a) Transverse slice of live E10.5 Venus::HES5 homozygous knock-in mouse showing the ventral HES5 domain in spinal cord ex vivo (left panel); Draq5 live nuclear stain with nuclear segmentation overlay (right panel); scale bar 30 µm. **(b)** Venus::HES5 nuclear signal corresponding to tissue in **(a)** obtained by applying nuclear segmentation onto Venus channel. **(c)** Pseudo-color look-up table applied to mean nuclear Venus::HES5 intensity (Materials and Methods) corresponding to segmented image in **(b).** Black line surrounding representative microclusters. **(d)** Distribution of sizes of microclusters of cells with high and similar levels of HES5 in dorso-ventral axes (left panel) and apical-basal (right panel); data consists of 25 microclusters measured from 9 slices and 3 independent experiments. **(e)** Pearson correlation coefficient observed in segmented E10.5 homozygous Venus::HES5 spinal cord ex-vivo slices showing correlation between mean nuclear Venus::HES5 intensity in any cell compared to its nearest neighbours (see Methods); dots indicate average per slice; bars indicate mean and standard deviation of 5 slices from 3 experiments (dataset is different from **(d)**).**(f)** Pearson correlation coefficient of mean nuclear Venus::HES5 intensity in relationship to distance; red dots indicate average Venus::HES5 correlation per slice of 12 slices from 3 experiments with corresponding red line indicating polynomial fit (order 2); gray dots with black line indicate correlations and polynomial fit from 5 randomizations of intensities analysed in the same way (see Methods). **(g)** Transverse slice of live E10.5 Venus::HES5 homozygous knock-in mouse showing the ventral HES5 domain in spinal cord ex vivo (left panel) with scale bar 30 µm; nuclear segmentation of Draq5 nuclear stain

applied to Venus::HES5 signal and pseudo-color look-up table applied to mean nuclear Venus::HES5 intensity (right panel); centre of intensity shown with *. **(h)** Representative example of Venus::HES5 intensity as a function of radial distance with respect to center of intensity (see Methods); red-line shows experimental data, coloured lines from theoretical radial gradients (a values denote strength of radial gradient). (**i)** Pearsons correlation coefficient of mean nuclear Venus::HES5 intensity with distance after subtraction of radial gradient in Venus::HES5 intensity; red dots represent average in each of 12 slices from 3 experiments.

Figure 2. HES5 microclusters are spatially periodic along dorsal-ventral axis of spinal cord.

(a) 20x snapshot of an ex-vivo slice culture of E10.5 spinal cord from Venus::HES5 heterozygous knock-in mouse, transverse section; delineated region (blue) correspond to data shown in (**b-c**). (**b)** Spatial profile of Venus::HES5 intensity averaged over 2.5hrs with 0 distance representing the ventral end of kymograph; black line represents the trend in Venus::HES5 data across the domain (see Methods). **(c)** Detrended spatial profile of Venus::HES5 corresponding to data shown in **(b)**. **(d)** Lomb-Scargle Periodogram analysis of detrended Venus::HES5 data in (**c**); horizontal lines show significance levels, green p=0.0001. purple p=0.01 , yellow p=0.1, red p=0.5; significant peaks>0.01.**(e)** Auto-correlation analysis of detrended Venus::HES5 spatial profile in **(c)** with multiple peaks indicating spatial periodicity; significant peaks (red arrowhead) lie outside gray area indicating 95% significance based on bootstrap approach (see Methods) and non-significant peaks (black arrowhead). **(f)** Representative example of auto-correlation from detrended Draq5 nuclear signal with peak to peak distances indicative of inter-nuclear distance in live tissue; gray area denotes 95% confidence area for Draq5. **(g)** Schematic of multiple non-overlapping regions of interest identified as Apical, Intermediate and Basal in the spinal cord tissue; width of regions in the apical-to-basal direction was 15µm. **(h)** Peak to peak distance in auto-correlation of detrended Venus::HES5 spatial profile corresponding to Apical, Intermediate and Basal regions of spinal cord; markers indicate average distance per experiment with a minimum of 3 z-stacks per experiment and 2 repeats (left and right of ventricle) analysed per z-stack; bars indicate mean and SD of 6 independent experiments; 2 tailed paired t-test with statistical significance levels p=0.0362* and p=0.0065**. **(i)** Spatial periodicity quantified as Venus::HES5 peak to peak spatial distance shown in **(h)** represented as average number of cells observed along dorsal-ventral axis.

Figure 3. HES5 protein is expressed in a dynamical spatial periodic pattern modulated by Notch.

(a) Schematic of extracting kymograph information from tissue data by averaging Venus::HES5 intensities observed in E10.5 heterozygous spinal cord slices to generate one intensity profile in the dorsal-ventral axis per timepoint (see Methods). **(b)** Representative kymograph data showing spatiotemporal Venus::HES5 expression profile along ventral-dorsal direction in a 15μm wide apical region and observed over 14h; local bands of 20μm width in D-V marked * and ** are indicative of low to high and high to low activity in the same area respectively. **(c)** Hierarchical clustering of apical Venus::HE5 expression from one representative experiment showing behaviour in the same area over time**;** columns represent fluctuations in Venus::HES5 intensity in small local areas (bands) obtained by dividing the spatial signal into non-overlapping 20μm regions and normalizing to the mean and standard deviation of each region over time (z-scoring see Methods); rows indicate timepoints; markers * and ** indicate regions corresponding to **(b)**. **(d)** Persistence of Venus::HES5 in 20μm regions expressed as continuous time intervals when signal in the band is high or low compared to its mean (see Methods); individual datapoints (gray) indicate quantification of high and low persistence time obtained from over 300 thin bands collected from multiple tissues with 2 z-stacks per tissue and 2 repeats (left and right of ventricle) per z-stack; dots indicate paired medians of 6 independent experiments; statistical test is paired t test of median per experiment with p=0.2406. **(e)** Ratio measure indicating time interval at high HES5 over time interval spent in low HES5 observed in apical 20μm bands; markers indicate ratios collected from over 300 bands also shown in **(d)**; bars indicate median and inter-quartile range. **(f)** Dynamics of detrended Venus::HES5 signal in the apical region generated by averaging kymograph data in **(b)** over 2h time intervals starting from time 0. **(g)** Schematic indicating the correspondence between Venus::HES5 spatial oscillator represented as detrended level and phase angle characteristics; the spatial oscillator traverses repeated cycles including start (HES5 low-blue arrowhead), middle (HES5-teal arrowhead) and end (HES5 low-yellow arrowhead) which in phase space corresponds to phase angles 0, π and 2π respectively. **(h)** Spatial phase map corresponding to spatial data in **(f)** obtained using the Hilbert transform (see Methods); columns indicate timepoints and rows indicate distance from Ventral to Dorsal direction; phase resets are visible as sharp drops in phase angle from 2π to 0 in the same area.

Figure 4. Notch inhibition increases HES5 pattern persistence.

(a) Start:Finish Venus::HES5 intensity ratio in E10.5 Venus::HES5 heterozygous spinal cord slices treated with control (DMSO) and Notch inhbitor DBZ (2 μM) observed over 16h; bars indicate mean and standard deviation of DMS0 (n=3 experiments) and DBZ (n=4 experiments); 2-tailed t-test p=0.0001. (**b)** Spatial peak to trough fold-change in Venus::HES5 intensity profile in the D-V axis over time measured in DMSO and DBZ treated E10.5 Venus::HES5 spinal cord slices; dots indicate average per z-slice; bars indicate median per condition; pairwise Kruskall-Wallis test p=0.0235* and p=0.0092** . (**c)** Percentage of ex-vivo slices with significant spatial period detected after 10-12hrs of DMSO and DBZ conditions; significant spatial period defined as multiple significant peaks in auto-correlation detected above the 95% confidence bounds; dots indicate % per experiments; bars denote median and inter-quartile range of DMS0 (n=3) and DBZ (n=4) experiments; 1 tailed t test p=0.0062**. (**d)** Peak to peak distance in auto-correlation plots of detrended Venus::HES5 spatial profile in DMSO and DBZ treated E10.5 Venus::HES5 spinal cord slices; gray dots represent significant mean peak-to-peak distance of DMSO (100) and DBZ (105) auto-correlation functions collected from 3 z-stacks per slice and 2 repeats (left and right of ventricle) with multiple timepoints; bars indicate median per experiments from DMSO (n=3) and DBZ (n=4) experiments; 2 tailed Mann-Whitney test p<0.0001. (**e)** Representative spatiotemporal plots of the detrended Venus::HES5 pattern along ventral-dorsal direction (0 to 200μm) in Untreated, DMSO and DBZ conditions obtained by averaging kymographs data in the same region over 2 hr time intervals. (**f)** Representative phase maps of spatial periodic Venus::HES5 intensity obtained using the Hilbert transform (see Methods) from data shown in **(e)**. **(g)** Phase synchronisation parameter of the detrended Venus::HES5 spatial oscillator over time in E10.5 Venus::HES5 spinal cord slices treated in DMSO vs DBZ conditions; dots indicate DMSO (21 kymographs, n=3 experiments) and DBZ (19 kymographs, n=4 experiments); 2 tailed Mann-Whitney test p=0.0207*.

Figure 5. Multicellular cell-cell coupling model explains the emergence of microclusters.

(a) Schematic of repressive interactions via Notch-Delta between neighbouring cells whereby the effects of HES5 protein in Cell 1 (marked as P_1) on transcription in Cell 2 and vice-versa are represented using an inter-cellular Hill function $J\left(P_{1,2}(t-\tau_{ND})\right)$ where t denotes time and τ_{ND} represents the intercellular time delay, the time interval required to synthesise the intermediate molecular species (detailed in **Supp. Fig 5a**); HES5 auto-repression is represented using an intra-cellular Hill function $G\left(P_{1,2}(t-\tau_H)\right)$ where τ_H represents the inter-cellular time delay, the time interval required for protein to be produced

and repress its own transcription. **(b)** Mathematical description of the inter-cellular Hill function and its parameters: time delay (τ_{ND}), repression threshold (P_0) and Hill coefficient (n); (bottom left panel) higher P_0 corresponds to reduced inter-cellular repression (i.e. decreased coupling strength) and conversely lower P_0 corresponds to higher coupling strength; (bottom right panel) increasing values of n correspond to increased steepness of the inter-cellular response. **(c)** Multiscale coupled mathematical model of the tissue environment consisting of a 2D hexagonal grid of cells expressing HES5 protein with corresponding auto-repression (described in **(a)**) coupled together by repressive interactions between its 6 immediate neighbours (see Methods); single cell inter-cellular repression is a Hill function (with parameters described in (**b)**) dependent on mean protein abundance in the neighbouring cells. **(d)** Parameter exploration of single cell temporal period emerging from the model at different repression threshold and time delay values. **(e)** Parameter exploration of phase synchronisation quantified using the Kuramoto Order Parameter (see Methods) where 1 indicates global in-phase activity and 0 indicates random phase relationship between cells. **(f)** Parameter selection strategy combining experimentally determined temporal phase (insert left panel) and KOP (insert right panel) values in spinal cord tissue (see (Manning *et al.*, 2019) and Methods) to indicate areas where model statistics (i.e. mean temporal period and KOP of synthetic data) resemble real tissue; values within ±1SD and 2±SD from the mean of the tissue are identified and values found outside of ±2.4SD from the mean of tissue are excluded. **(g)** Representative examples of synthetic kymograph data obtained at specific levels of repression threshold: *Salt and Pepper* ($P_0 = 400$), *Global in phase* ($P_0 = 15000$) and *Local in phase* ($P_0 = 21000$) and corresponding KOP values; the presence of microclusters at weak coupling is indicated with red arrowheads; time delay 150min, $n = 4$. **(h)** Kymograph data obtained in the absence of coupling between cells; phase relationships are random with low KOP. **(i-j)** Synthetic data timeseries corresponding to simulations in **(g)** showing the behaviour of 3 neighbouring cells over time.

Figure 6. Cell-cell coupling strength can regulate probability of differentiation in a multicellular environment.

(a) Representative synthetic timeseries example and mathematical description of probability of differentiation (P_{diff}) in relation to population mean HES5 protein levels (referred to as 'differentiation threshold', D_{thresh}) whereby HES5 protein abundance ($P(t)$) dropping below the threshold increases the rate at which cells differentiate. **(b)** Differentiation rates estimated from the multicellular coupled model (detailed in **Figure 5)** over a wide range of repression threshold values corresponding to decreasing coupling strength; three dynamic regimes are

labelled as *Salt and Pepper*, *Global in phase* and *Local in phase* mirroring examples shown in **Figure 5g,i**. **(c)** Analysis of temporal CoV and spatial CoV from synthetic data corresponding to differentiation rates shown in **(b)**; these statistics indicate that spatial variability correlates better with differentiation rates meanwhile temporal variability shows only a moderate quasi- linear increase in *Salt and Pepper* conditions compared to the rest. Single cell parameters used to generate **(b)** and **(c)** are shown in **Supplem Table 1 Main**, and the multicellular parameters used were $n_{ND} = 4$, $\tau_{ND} = 150$ minutes. Each value plotted in **(b)** and **(c)** shows the mean and SD from 10 simulations at each repression threshold value.

Figure 7. Type of HES5 spatial pattern correlates with rate of differentiation in motorneuron and ventral interneuron domains.

a) Transverse cryosection of E10.5 Venus::HES5 spinal cord. Venus::HES5 endogenous signal, OLIG2 – motorneuron progenitor marker, NGN2 – early marker of neuronal commitment. Scale bar 20 µm. **b)** Relative nuclear intensities of Venus::HES5 and NGN2 in motorneuron and interneuron progenitors. Bars show mean and SD of at least 494 cells per domain from 5 slices in 2 experiments. Kruskal-Wallis with Dunn's multiple comparison test. adjusted p-values ** p=0.0032, ***p<0.001. **c)** Pseudo-color look-up table applied to mean nuclear Venus::HES5 intensity within motorneuron (MN) and interneuron (IN) domains, corresponding to segmented image in **(a).** Black line surrounding representative microclusters. **(d)** Distribution of sizes of microclusters of cells with high and similar levels of HES5 in dorso-ventral axes for MN and IN domains; data consists of 34 microclusters measured from 5 sections and 3 independent experiments. **e)** Peak to peak distance in auto-correlation plots of de-trended Venus::HES5 spatial profile in MN and IN domains. This is a measure of spatial period in Venus::HES5 profile along dorsal-ventral axis of spinal cord. Grey data points represent mean peak to peak distance of at least 3 slices with left and right ventricle analysed separately in 6 experiments. Black dots show median per experiment and line shows overall median. 2-tailed Mann-Whitney test. Approx. p-values **** p<0.00001. **f)** Fold-change in Venus::HES5 spatial pattern between hi-low regions in IN domain relative to MN domain. Data points represent mean per experiment. Lines shows mean and SD of 6 experiments. 2-tailed Mann-Whitney test. Approx. p-values ** p=0.0022.

Figure 8. Coupling strength determines rate of differentiation through changes in spatial patterning. Through a combination of experimental and computational work we characterised that HES5 dynamic expression in the mouse E10.5 ventral spinal cord. We found evidence that progenitors located in two domains (motorneuron, MN and interneuron,

IN) give rise to distinct spatiotemporal characteristics that are indicative of differences in coupling strength and can explain increased differentiation rates observed in MN.

Supplementary Figure Legends

Supplementary Figure 1. Venus::HES5 expression in single progenitor cells located in the ventral domain of spinal cord. Related to Figure 1.

(a) Transverse slice of live Venus::HES5 homozygous knock-in mouse spinal cord E10.5 ex vivo, Draq5 live nuclear stain and brightfield image. Scale bar 50µm. (**b)** Immunofluorescence of E10.5 Venus::HES5 transverse slice of spinal cord ex-vivo. SOX2+ progenitors and endogenous Venus::HES5 signal. Scale bar 40 µm. **(c)** Viridis look-up table applied to mean nuclear Draq5 intensity corresponding to transverse slice in **Figure 1c**. **(d)** Correlation coefficient of mean nuclear Venus::HES5 intensity with distance for a representative single E10.5 homozygous Venus::HES5 spinal cord ex-vivo slice. Black line denotes coefficients from real data and colored lines show 5 randomisations of the mean intensities per slice.(**e**) Transverse slice of live Venus::HES5 homozygous knock-in mouse spinal cord E10.5 ex vivo showing segmentation of Draq5 live (left panel) and mask applied to Venus::HES5 channel (right panel) . Images correspond to slice shown in **Figure 1g**. **(f)** Viridis look-up table applied to mean nuclear Venus::HES5 intensity in **Figure 1g** after radial gradient removal.

Supplementary Figure 2. Draq5 and Venus::HES5 spatial periodicity in live spinal cord tissue cultures. Related to Figure 2.

(a) Transverse slice of live Venus::HES5 homozygous knock-in mouse spinal cord E10.5 ex vivo, Draq5 live nuclear stain; rectangle shows region for spatial profile. **(b)** Spatial profile of Venus::HES5 (black) and Draq5 (red) nuclear stain from region delineated in **(a)**; arrow shows region of Venus::HES5 low and Draq5 high indicating low Venus::HES5 areas are not nuclei free. **(c)** Auto-correlation plot of Venus::HES5 and Draq5 from the same tissue profile; black dashed lines show confidence limits for peak significance based on bootstrap approach on the intensity profile (see Methods); red triangle - significant peak, black triangle – non-significant peak; multiple significant peaks in auto-correlation shows periodicity in spatial profile. **(d)** Distribution of peak-to-peak distance in auto-correlation plots of Draq5 spatial profile; this is a measure of inter-nuclear distance in Draq5 profile along dorsal-

ventral axis of spinal cord; data points represent all peak to peak distances from 9 slices, 6 experiments. Mean 9.3 ± 0.42 µm (95% confidence limits). **(e)** Mean peak to peak distances per experiment in apical, medium and basal regions (10, 30 and 60 µm from ventricle respectively); lines indicate mean and SD per experiment; datasets consisted of at least 3 z-sections and both left and right sides of ventricle analysed in n=6 experiments.

Supplementary Figure 3. Kymograph analysis from Venus::HES5 expression in apical progenitors. (a) Kymographs of expression profiles along ventral-dorsal direction in a 15µm wide apical region. Panels indicate 5 example slice cultures in addition to example in **Figure 3b**. **(b)** Spatiotemporal plots of the de-trended Venus::HES5 pattern along ventral-dorsal direction. Generated by averaging kymographs every 2 hrs Venus::HES5 intensity is plotted in x-direction for each time point. 4 example slice cultures in addition to example in **Figure 3e**. **(c)** Spatial phase map of Venus::HES5 oscillator over time corresponding to spatiotemporal plots in **(b)**.

Supplementary Figure 4. Changes in Venus::HES5 spatiotemperal expression pattern in live slice cultures treated with Notch inhibitor DBZ. Related to Figure 4.

(a) Auto-correlation analysis of detrended apical Venus::HES5 spatial profile in DMSO (control) and DBZ (2 µM) treated E10.5 Venus::HES5 spinal cord slices**;** panels show auto-correlation of detrended Venus::HES5 signal averaged from 0-2h of timelapse video (top panels) and corresponding auto-correlation functions **i**n the same slices averaged in 2hr windows for 10h; we observed a decrease in amplitude of auto-correlation peaks over time in DBZ-treated slices. **(b)** Peak to peak distance in auto-correlation from spatial data shown in **Figure 4d** presented as median per experiment from DMSO (n=3 experiments) and DBZ (n=4 experiments); 1 tailed t test p=0.0526. **(c)** Nuclear density represented by the % area covered by nuclei in DMSO and DBZ treated ex-vivo E10.5 spinal cord slice cultures dots indicate multiple z-stacks from DBZ (5 slices) and DMSO (4 slices); bars indicate mean and SD per condition; 2 tailed t test p=0.0004***. **(d)** Representative examples of the detrended Venus::HES5 signal observed along ventral-dorsal direction in DMSO and DBZ conditions; Venus::HES5 intensity data obtained by averaging kymographs over 2 hrs intervals; panels represent individual slice cultures (2 per condition) in addition to examples in **Figure 4e**. (**e)** Spatial phase maps obtained from detrended Venus::HES5 signal in DMSO and DBZ conditions; panels correspond to Venus::HES5 intensity traces shown in **(d)** and are additional to examples shown in **Figure 4f.**

Supplementary Figure 5. Exploration of HES5 spatiotemporal dynamics in a multicellular environment.

(a) Diagram of Notch-Delta inter-cellular communication and HES5 interactions. Our model takes into account that HES5 negatively regulates its own mRNA production (gray highlighted area), downstream proneural genes and Delta; the direct and/or indirect (via proneural genes) repression of Delta by HES5 is expressed mathematically through the means of an inter-cellular Hill function (see Methods). (**b)** Quantification of phase synchronisation measured as Kuramoto Order Parameter (KOP) (see Methods) in sparsely tracked apical progenitor cells in live E10.5 spinal cord slices; gray dots indicate KOP values measured at individual timepoints between 0 to 12-14h with black dots indicating average per slice; bar represents mean of 3 experiments. **(c)** Explorations of the inter-cellular parameters determining the repressive interactions between cells via a Hill function (**Figure 5b)**: intercellular time delay (x-axes), repression threshold (y-axes), and Hill coefficient (plotted as separate maps in each column); pseudo-color indicates (top panels) average temporal period of HES5 oscillations (in hours) and (bottom panels) average KOP values from 5 independent simulations per parameter combination; statistics were collected from synthetic HES5 timeseries using a 26 by 10 grid size per simulation with length of 100 hours and generated using the stochastic model with randomised initial conditions. (**d)** Microcluster size measurements obtained from synthetic weakly coupled cells corresponding to repression threshold values between 20,000 to 24,000 (see Methods); dataset represents the frequency distribution of microclusters detected in 250 synthetic data kymographs of 80 hours length; **(e)** Inter-cellular parameter exploration of frequency of cluster detection (fraction of time points in a simulation where clusters are detected, see Methods); panels correspond to Hill coefficient values of 4 (top) and 6 (bottom); values observed within a weak coupling range are presented as frequency plots to the right. (f) Inter-cellular parameter exploration of spatial periodicity for Hill coefficient values 2 (top) and 4 (bottom); spatial periods (as cell number) found significant using a Fisher G significance test (see Methods). Statistics in **(e,f)** represent average of 5 independent simulations collected from a grid of 26 by 10 synthetic HES5 timeseries per simulation with length of 100 hours and generated using the stochastic model with randomised initial conditions.

Supplementary Figure 6. Extensive search over multiple single-cell parameter sets shows no additional model behaviour at lower coherence values.

Multi-parametric exploration of HES5 inter-cellular and intra-cellular dynamics used to investigate microcluster occurrence **(a)** and spatial periodicity **(b)**. Panels represent maps of

intercellular time delay (x-axes), repression threshold (y-axes), and Hill coefficient (plotted as separate maps in each column). Panels arrayed horizontally correspond to distinct HES5 auto-repression parameter sets marked as C15, C10 and C5 with 3 repeats (e.g. C15-1 to 3) corresponding to low coherence (15% to 5%) dynamics where low coherence indicates reduced oscillatory activity in the population. Parameter sets used are presented in **Supp. Table 1**. Pseudo-color indicates **(a)** frequency of cluster detection (fraction of time points in a simulation where clusters are detected, see Methods) and **(b)** spatial period (as cell number) found significant using a Fisher G significance test (see Methods); statistics were collected from synthetic HES5 timeseries using a 26 by 10 grid size per simulation with length of 100 hours and generated using the stochastic model with randomised initial conditions.

Supplementary Figure 7. Venus::HES5 spatial expression patterns in the interneuron and motorneuron domains.

(a). Transverse cryosection of E10.5 Venus::HES5 spinal cord. Venus::HES5 endogenous signal, OLIG2 – motorneuron progenitor marker, NGN2 – early marker of neuronal commitment, DAPI; scale bar 25 µm. **(b)** Spatial expression profile of Venus::HES5, NGN2 and OLIG2 from the same tissue to help delineate motorneuron (OLIG2+) vs interneuron (OLIG2-) domains. **(c)** Spatial profile of Venus::HES5 intensity (black) generated by averaging 2.5hrs of kymograph data; 0 distance represents ventral end of kymograph; blue dotted line is trend in Venus::HES5 data across the domain determined by polynomial fit; domain boundary between motorneuron progenitors (MN) and interneuron progenitors (IN) marked with red dashed line. **(d)** De-trended spatial profile of Venus::HES5 corresponding to **(c)** in motorneuron progenitors (red-MN) and interneuron progenitors (blue-IN). **(e)** Auto-correlation plot of de-trended Venus::HES5 spatial profile in MN and IN progenitors; black lines show confidence limits for peak significance based on bootstrap approach on de-trended Venus::HES5 intensity profile (see Methods); red triangle - significant peak, black triangle – non-significant peak; multiple significant peaks in auto-correlation shows periodicity in spatial profile of Venus::HES5 intensity. (**f)** Spatial periodicity in motorneuron vs interneuron domain measured with the Lomb-Scargle periodogram; top 2 significant peaks were used to calculate spatial period from 2 to 3 z-sections per experiment, left and right side of ventricle analysed separately and 6 experiments; bars indicate mean with SD; Mann-Whitney test with two-tail significance for $p<0.0001$****.

Supplementary Table 1. Model Parameters

Supplementary Movie 1

Live imaging of ex-vivo E10.5 Venus::HES5$^{+/-}$ spinal cord slice. Viridis look-up table of Venus::HES5 intensity in ventral expression domain of HES5. Frames taken every 15 mins for 12.25 hrs. Scale bar 50 µm.

Supplementary Movie 2. Time-course animation of the model grid output for various coupling strengths.

Simulation output in the form of a hexagonal grid of cells (26x10) where each hexagon represents an individual cell and the colour indicates the expression of HES5 in that cell (colour bar indicates the number of proteins being expressed and each simulation was run up to 100hrs). From left to right the repression threshold increases $P_{ND0} = 400, 15000, 21000, \infty$) and the other multicellular parameters are set to $\tau_{ND} = 150$min, $n_{ND} = 4$. In panel 1 (left), the coupling strength is the strongest, which results in the formation of salt and pepper spatial patterning (corresponding kymograph shown in **Figure 5g**). Panel 2 shows global in phase (corresponding kymograph shown in **Figure 5g**). Panel three shows local in phase where regions of locally synchronised cells can be seen (corresponding kymograph shown in **Figure 5g**). Panel 4 (right) shows the case when coupling between the cells is not present (corresponding kymograph shown in **Figure 5h**).

Figure 1. Microclusters of cells have positively correlated HES5 levels.

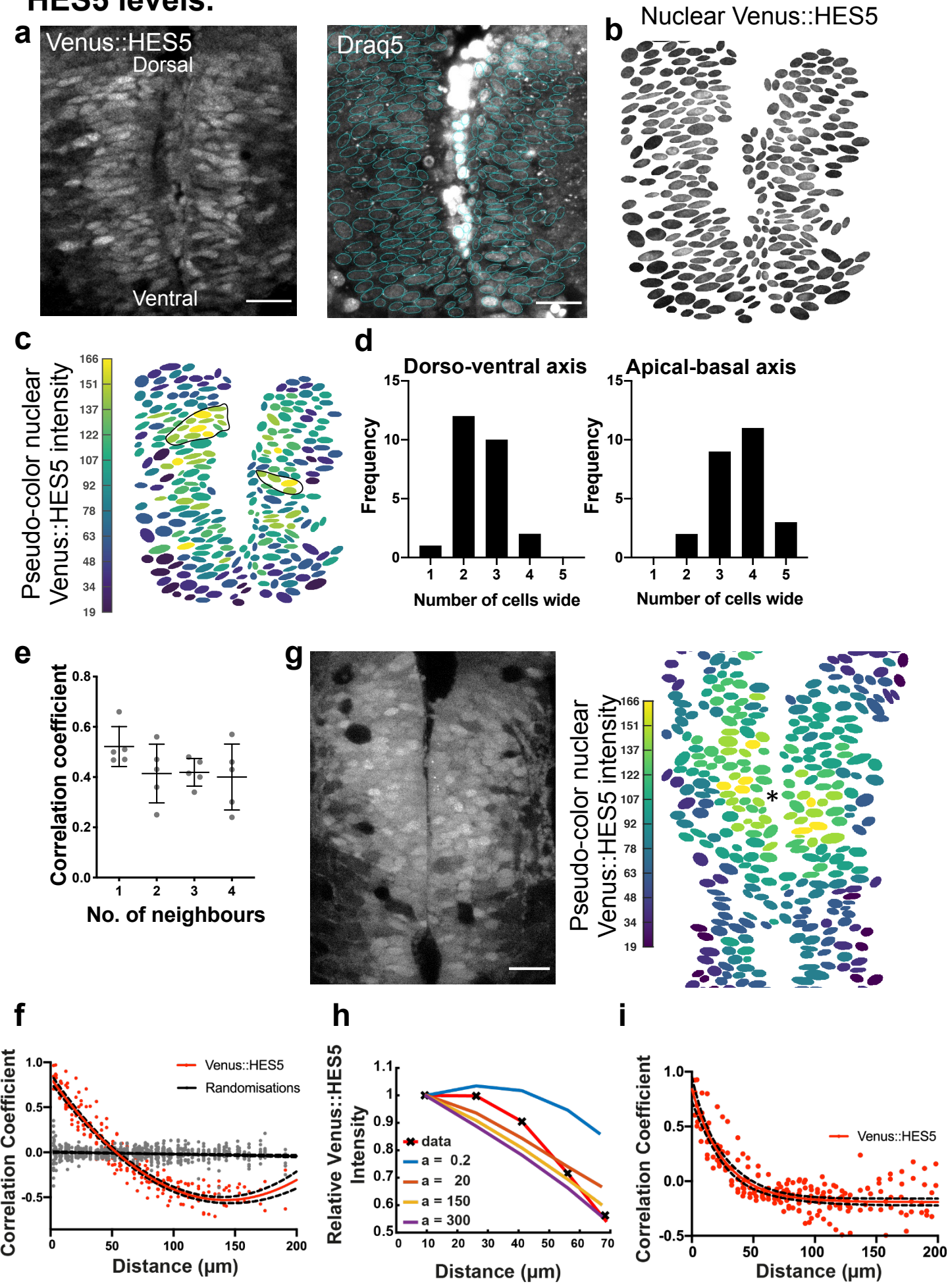

Figure 2. HES5 micro-clusters are spatially periodic along dorsal-ventral axis of spinal cord

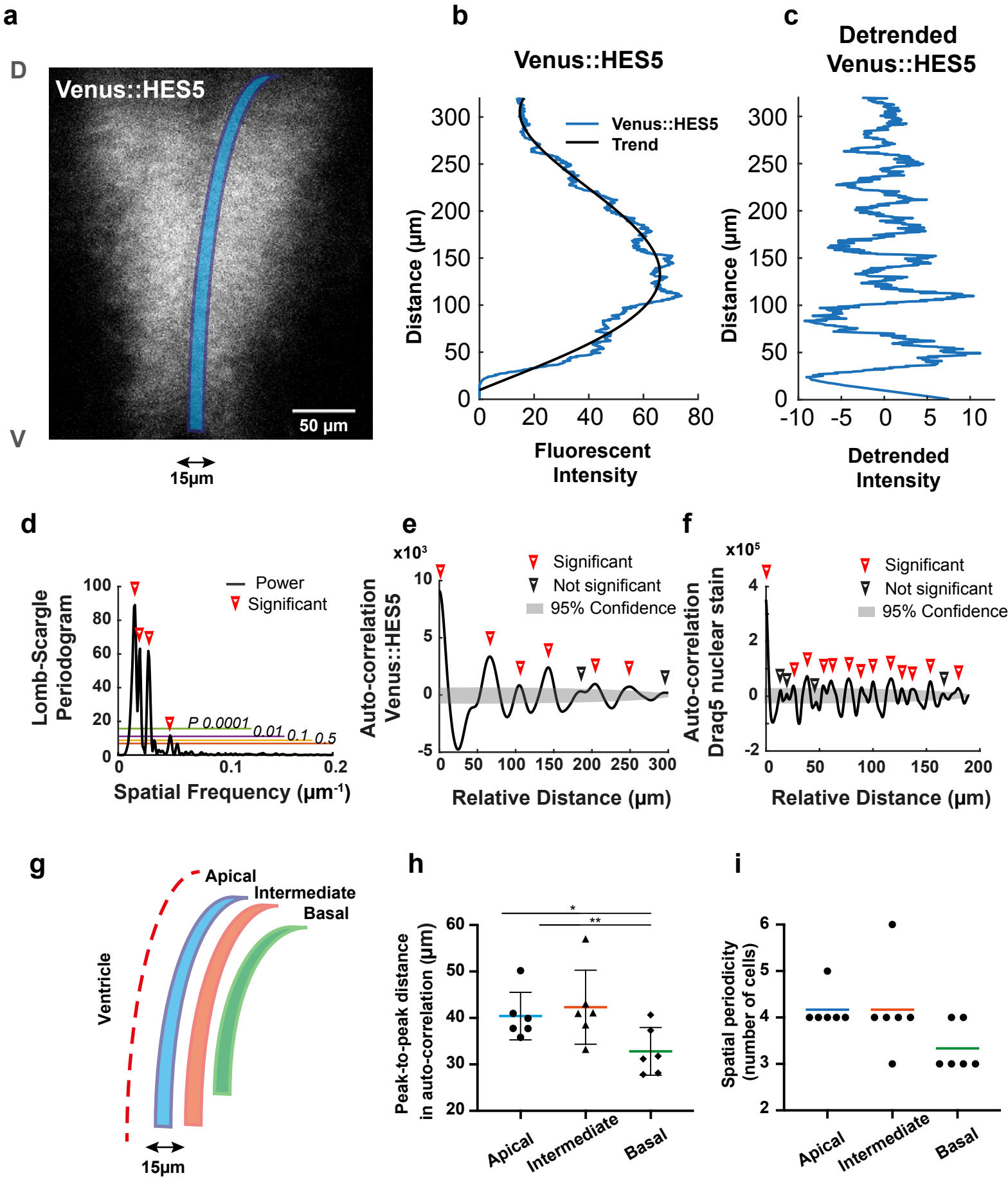

Figure 3. HES5 is expressed in a dynamically modulated pattern.

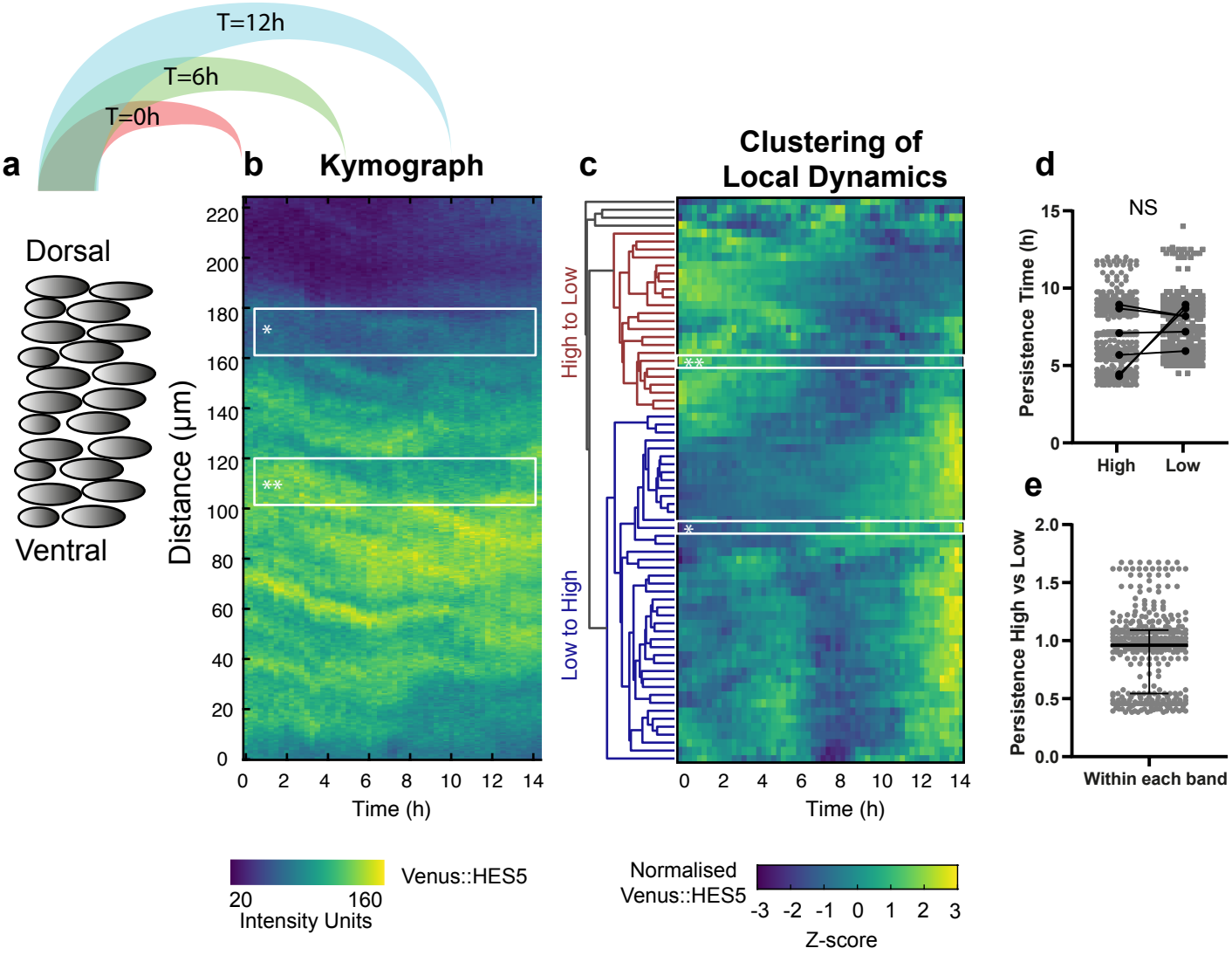

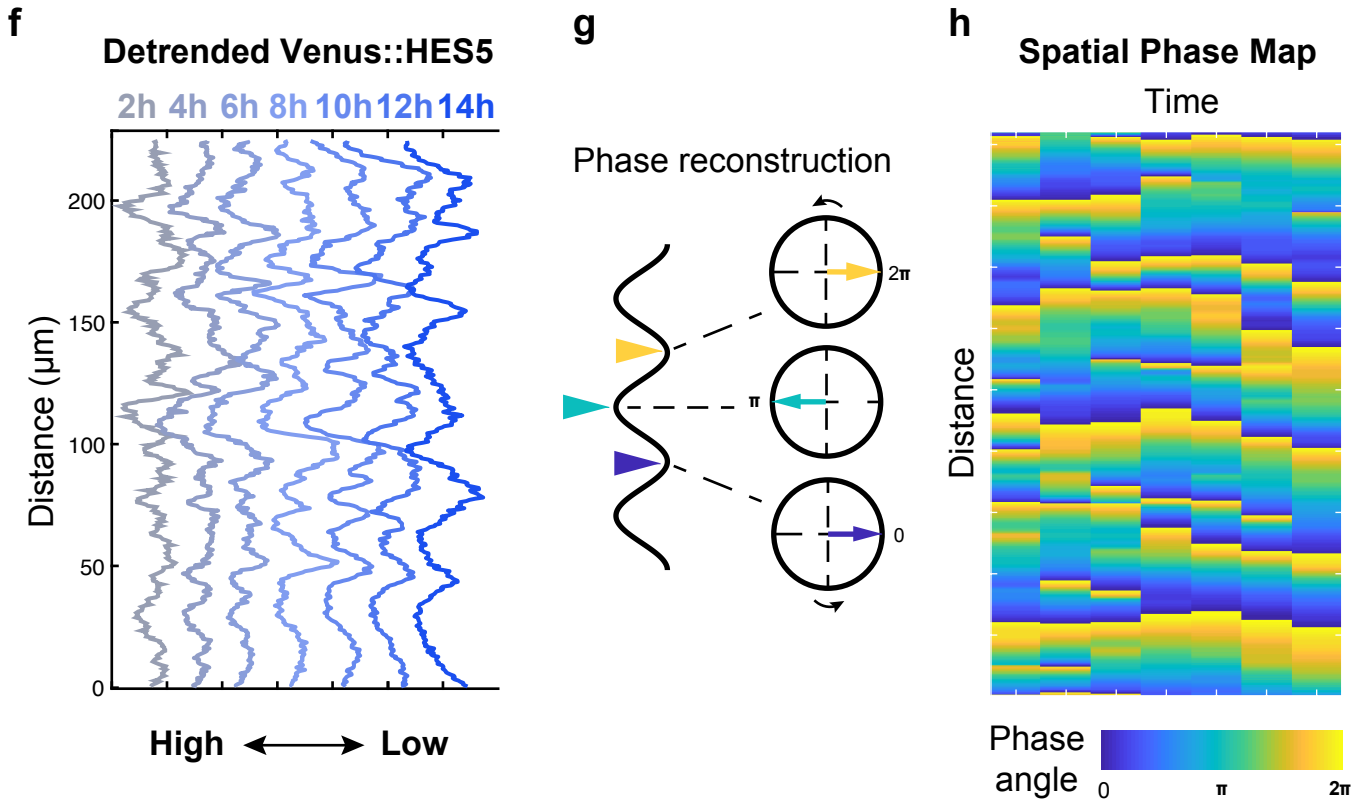

Figure 4. Notch inhibition increases HES5 pattern persistence.

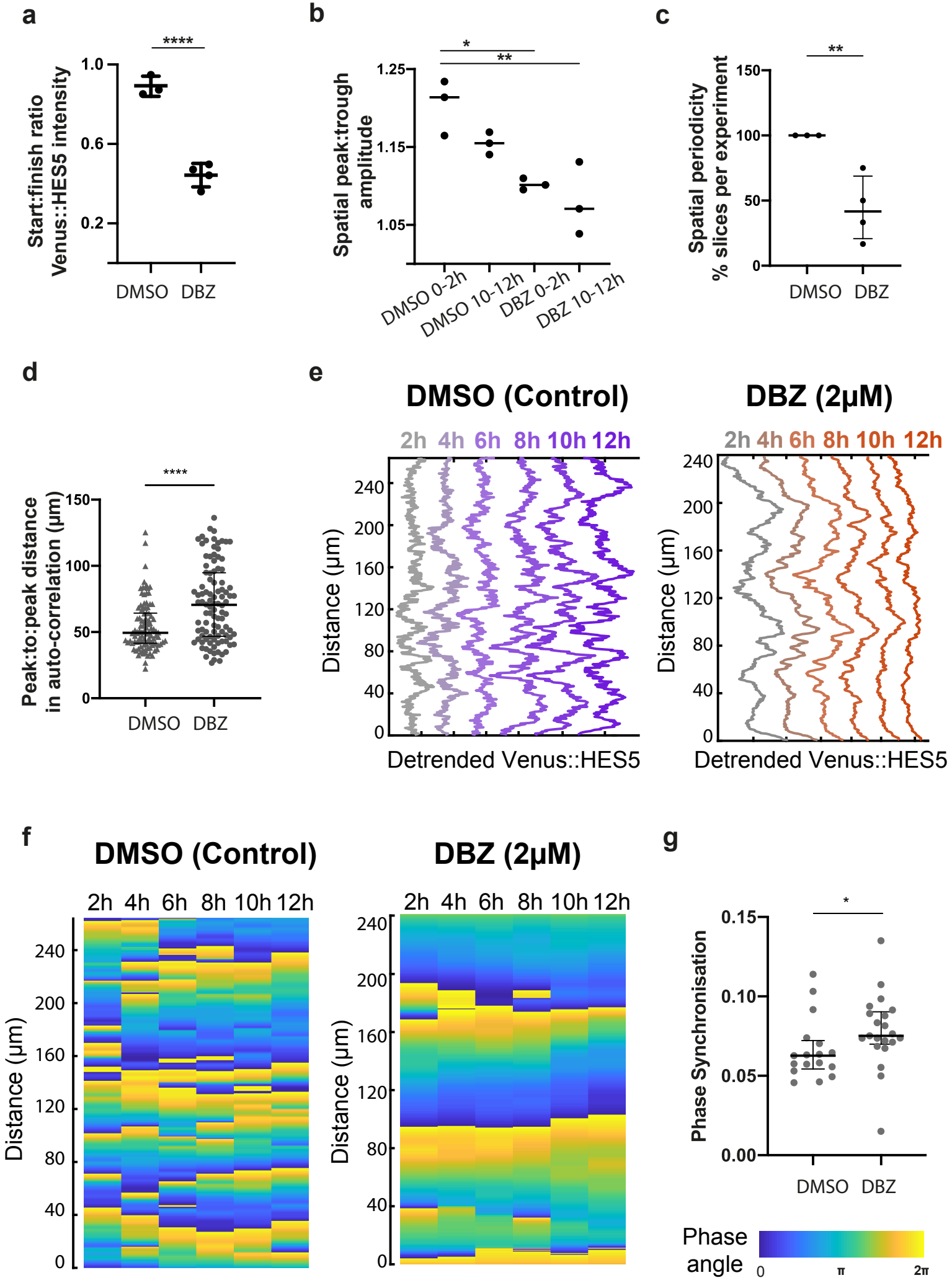

Figure 5. Mathematical model of cell-cell interactions explains the emergence of microclusters.

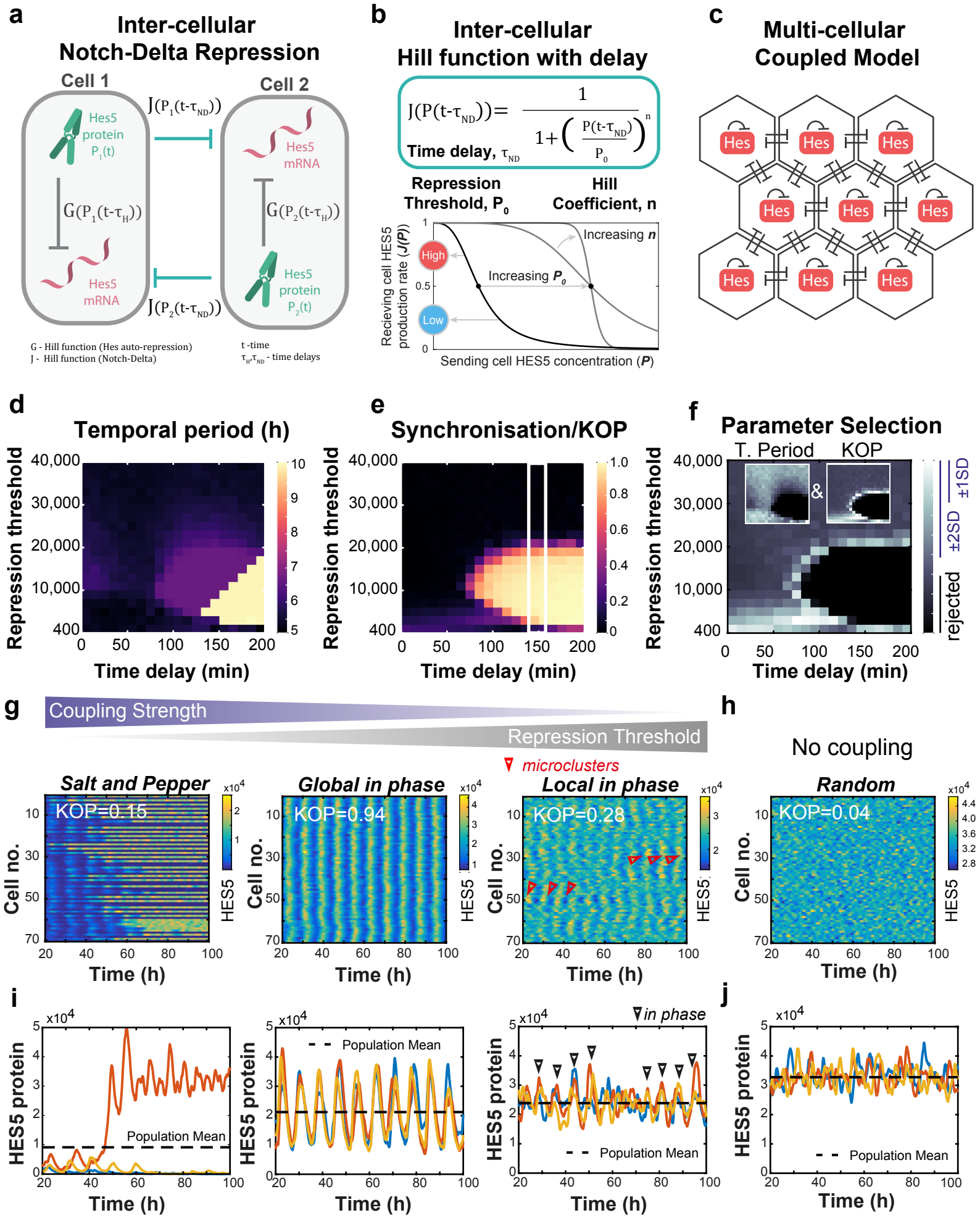

Figure 6. Cell-cell coupling strength can regulate probability of differentiation in multi-cell model

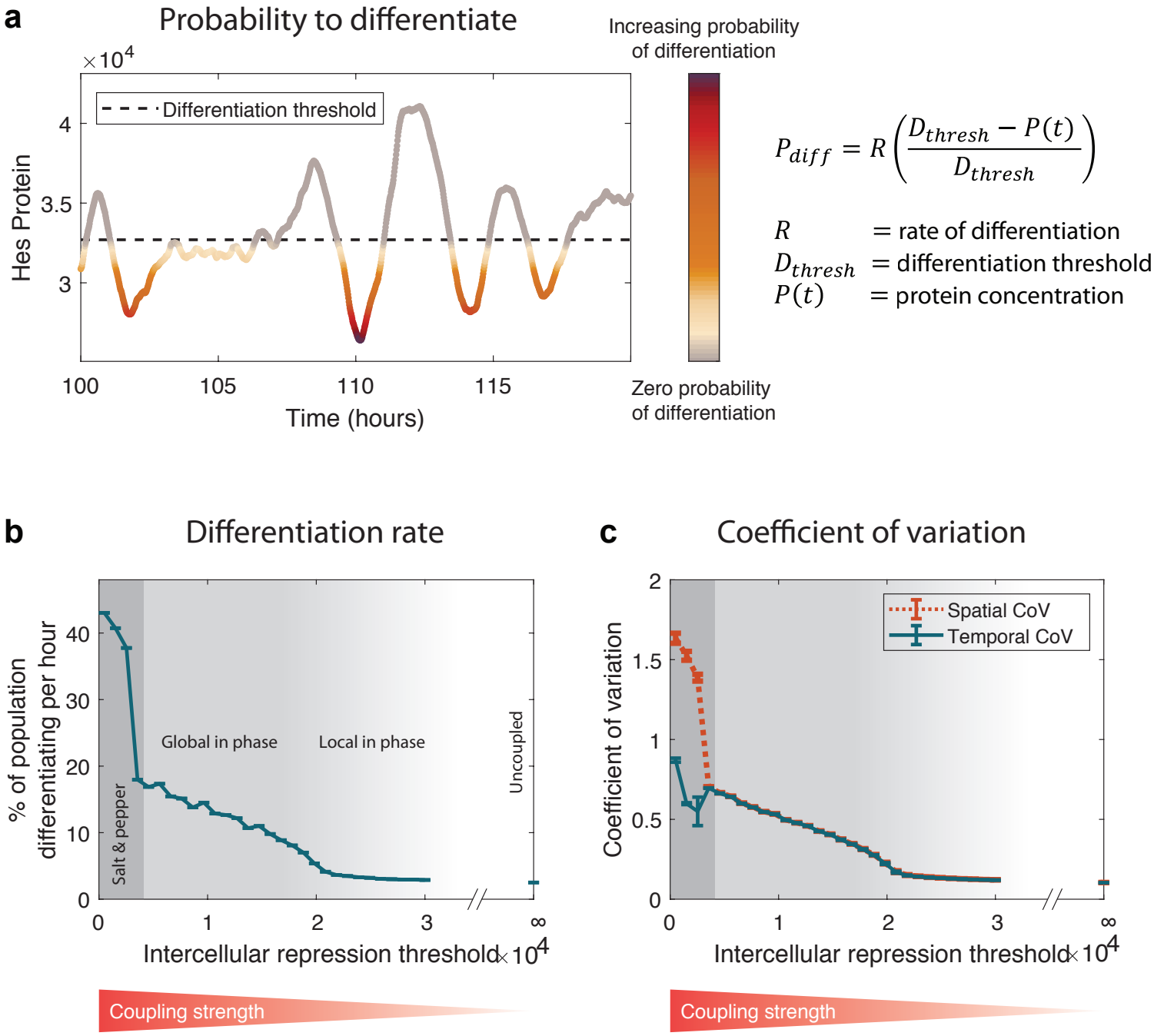

Figure 7. Type of HES5 spatial pattern correlates with rate of differentiation in motorneuron and ventral interneuron domains

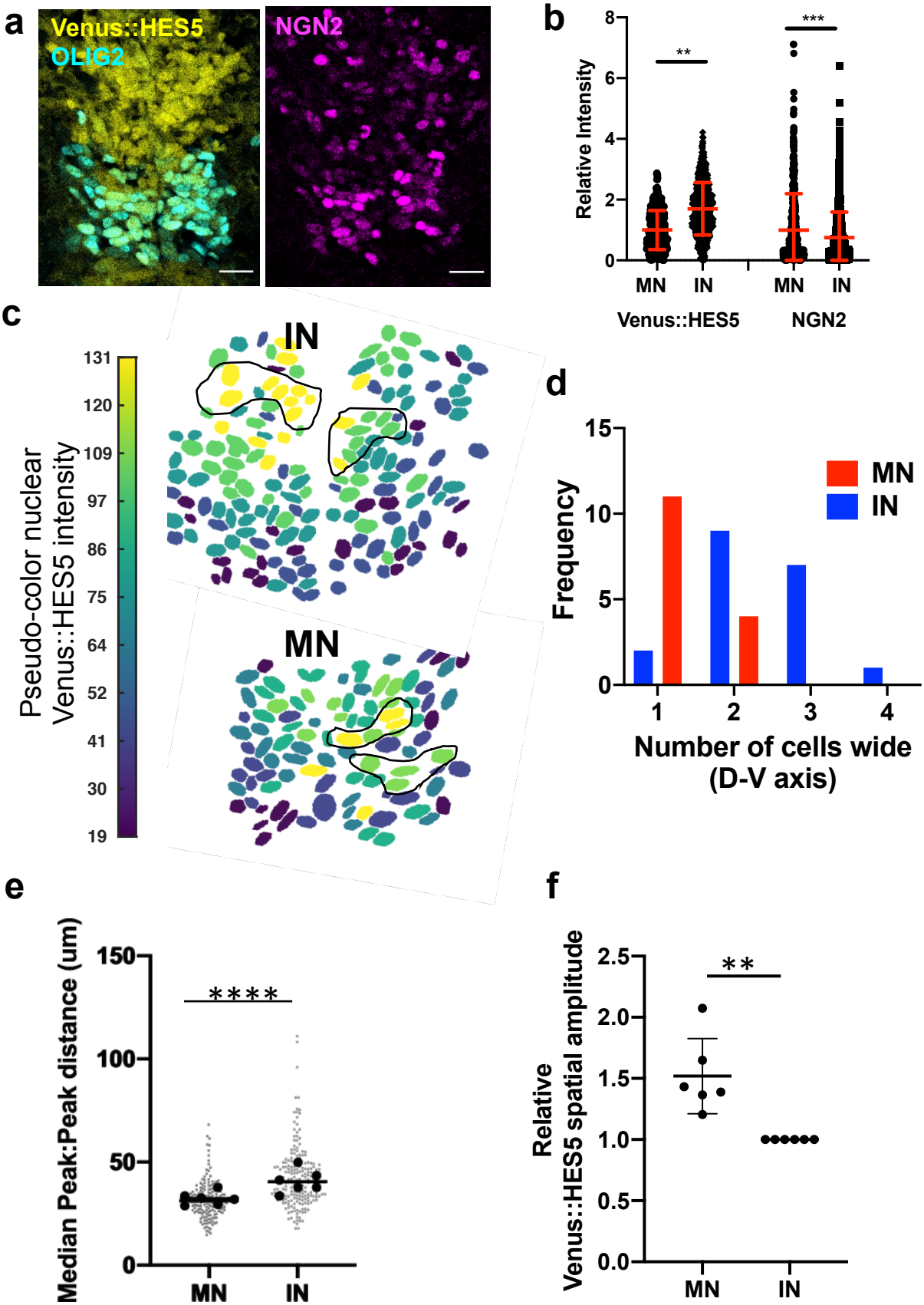

Figure 8. Coupling strength determines rate of differentiation through changes in spatial patterning

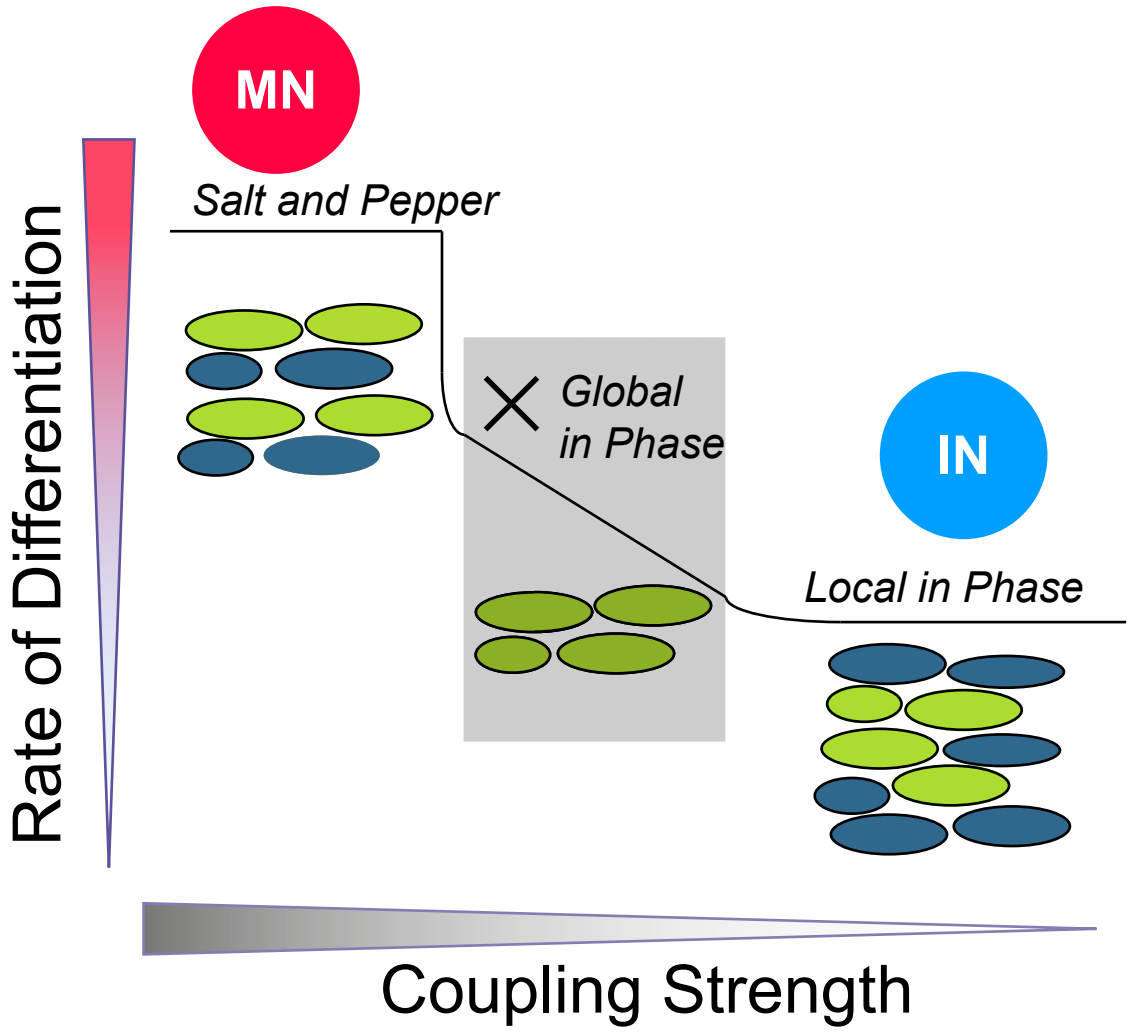

Supplementary Figure 1. Related to Fig. 1

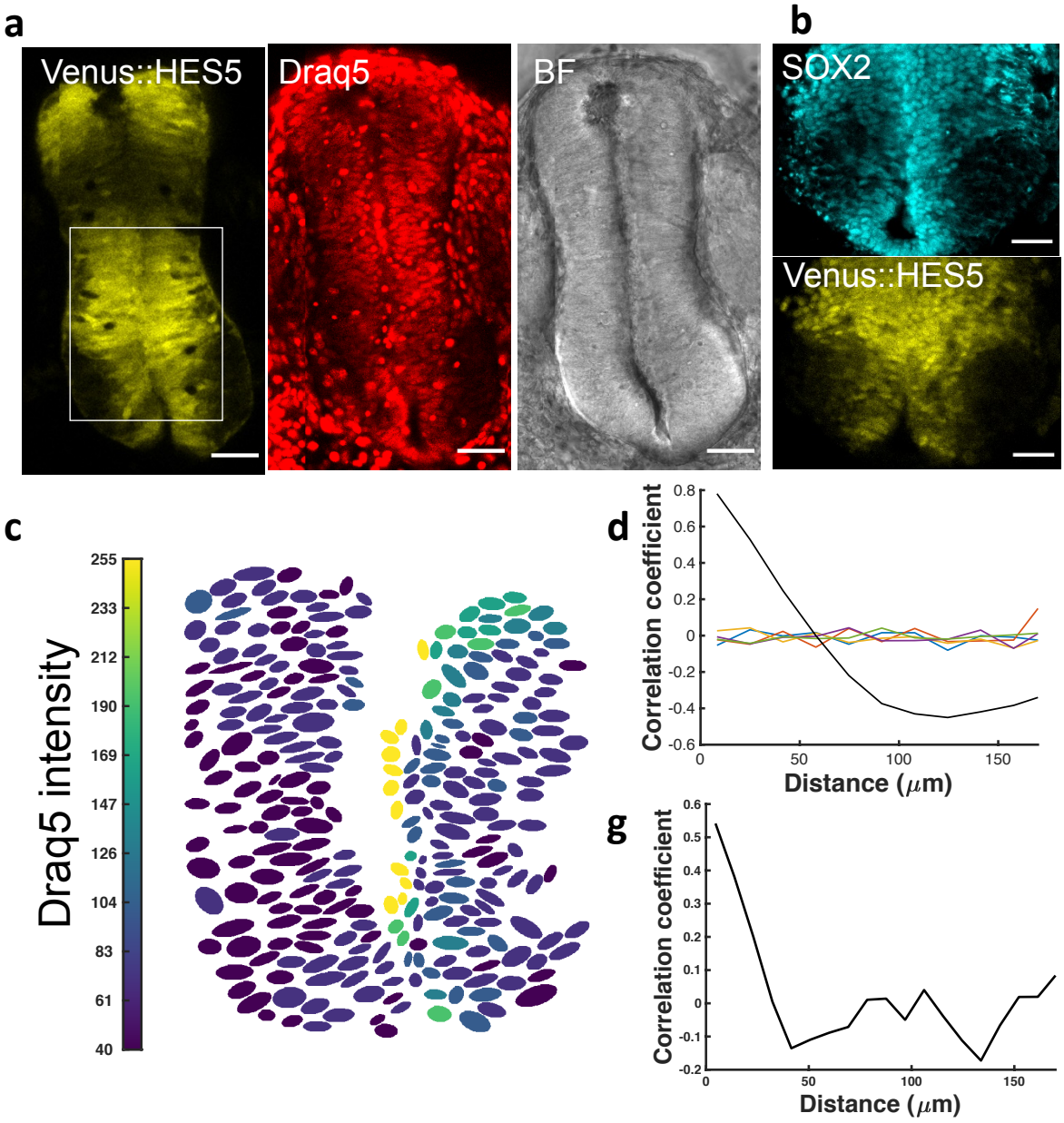

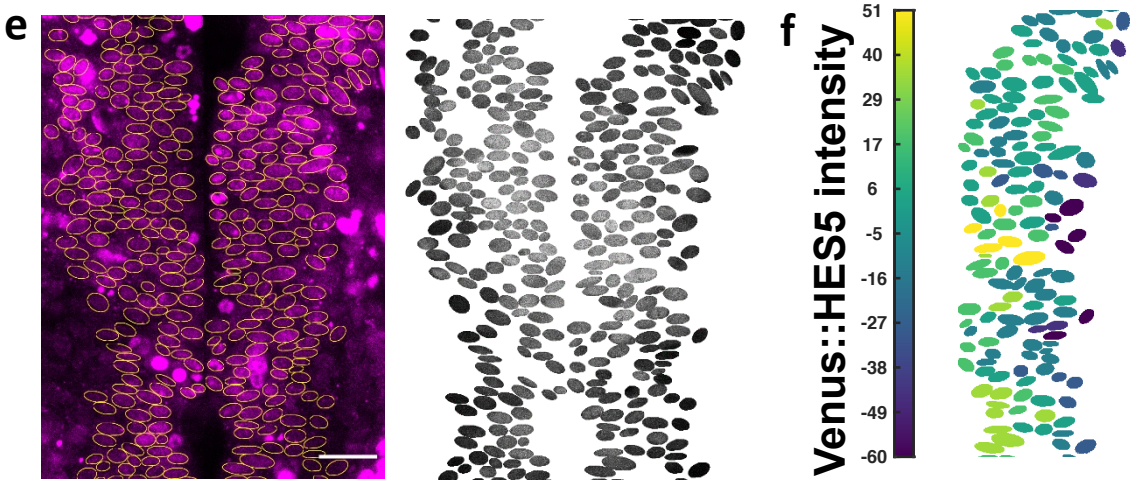

Supplementary Figure 2. Related to Fig. 2

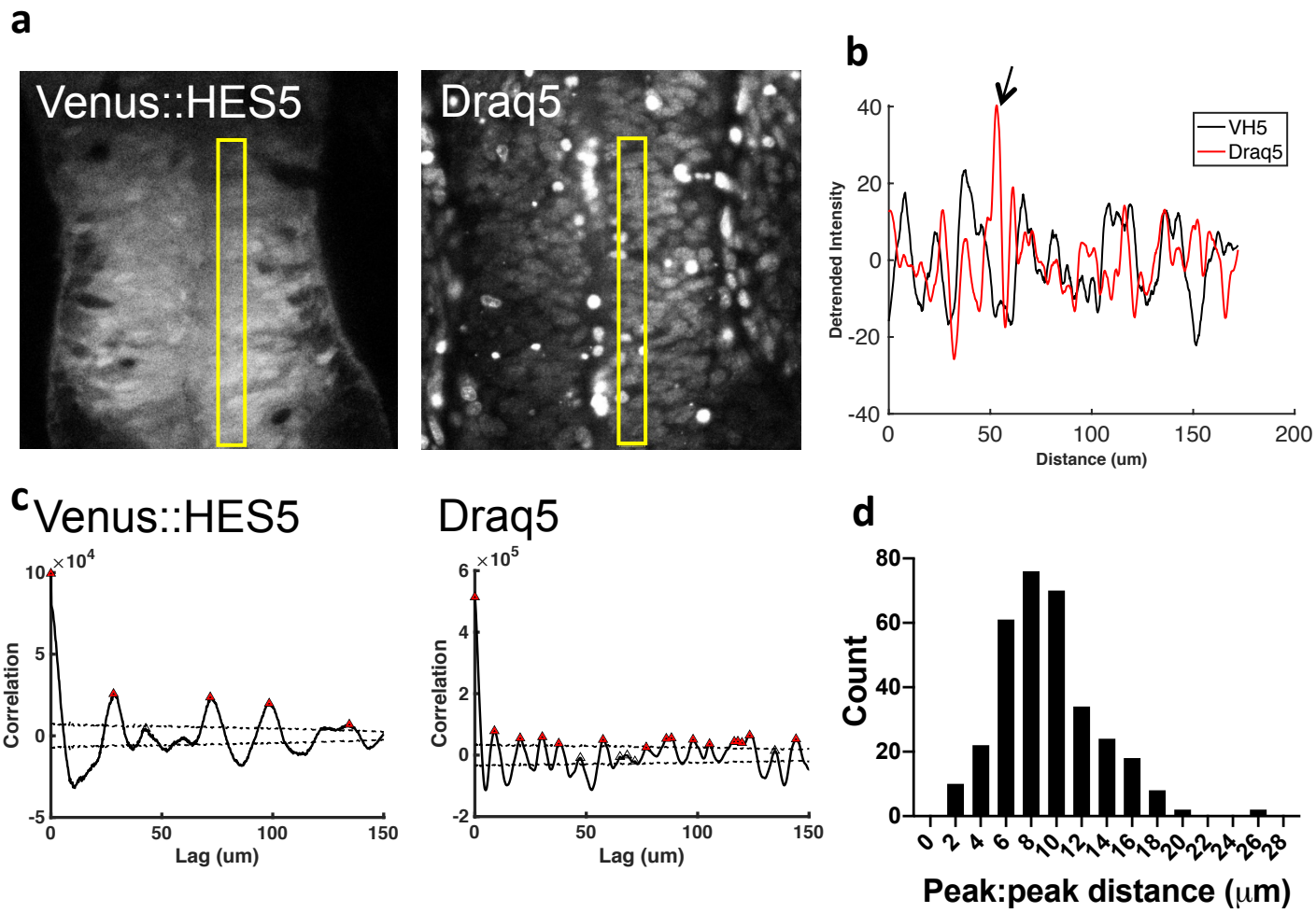

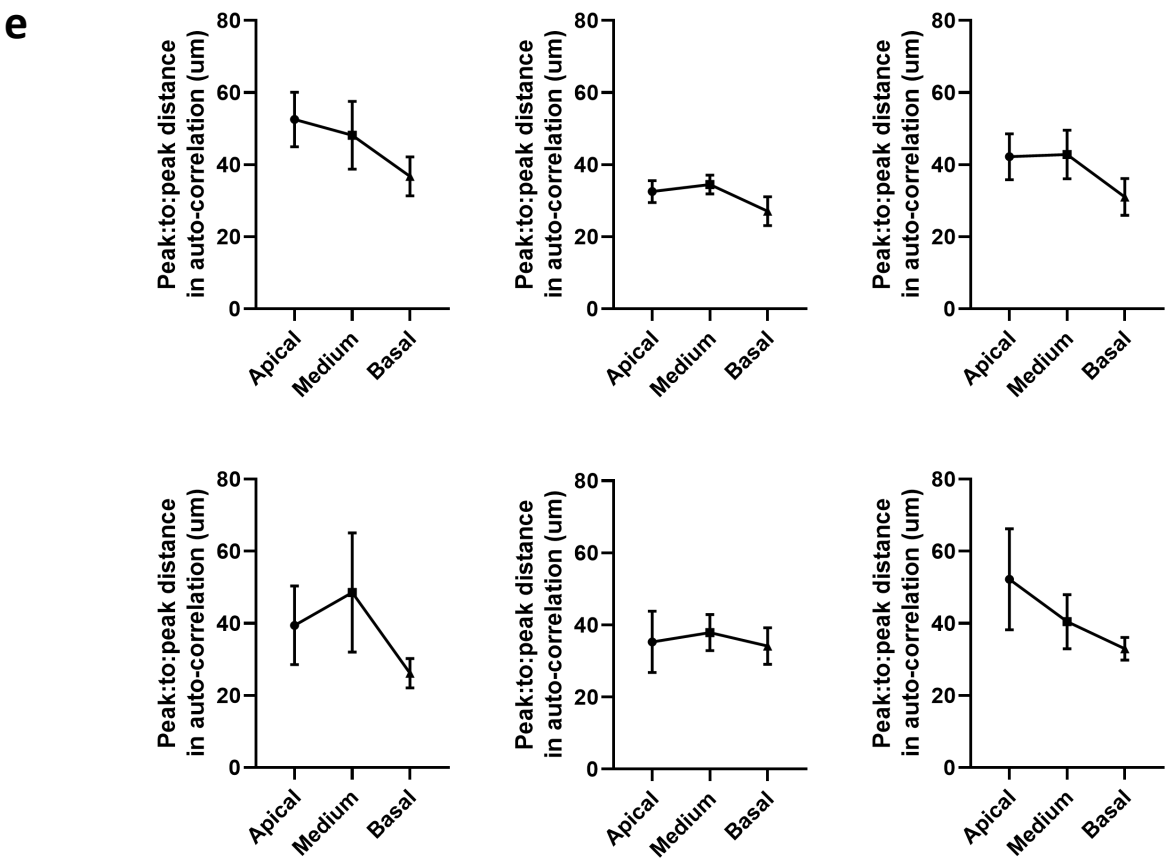

Supplementary Figure 3. Related to Figure 3.

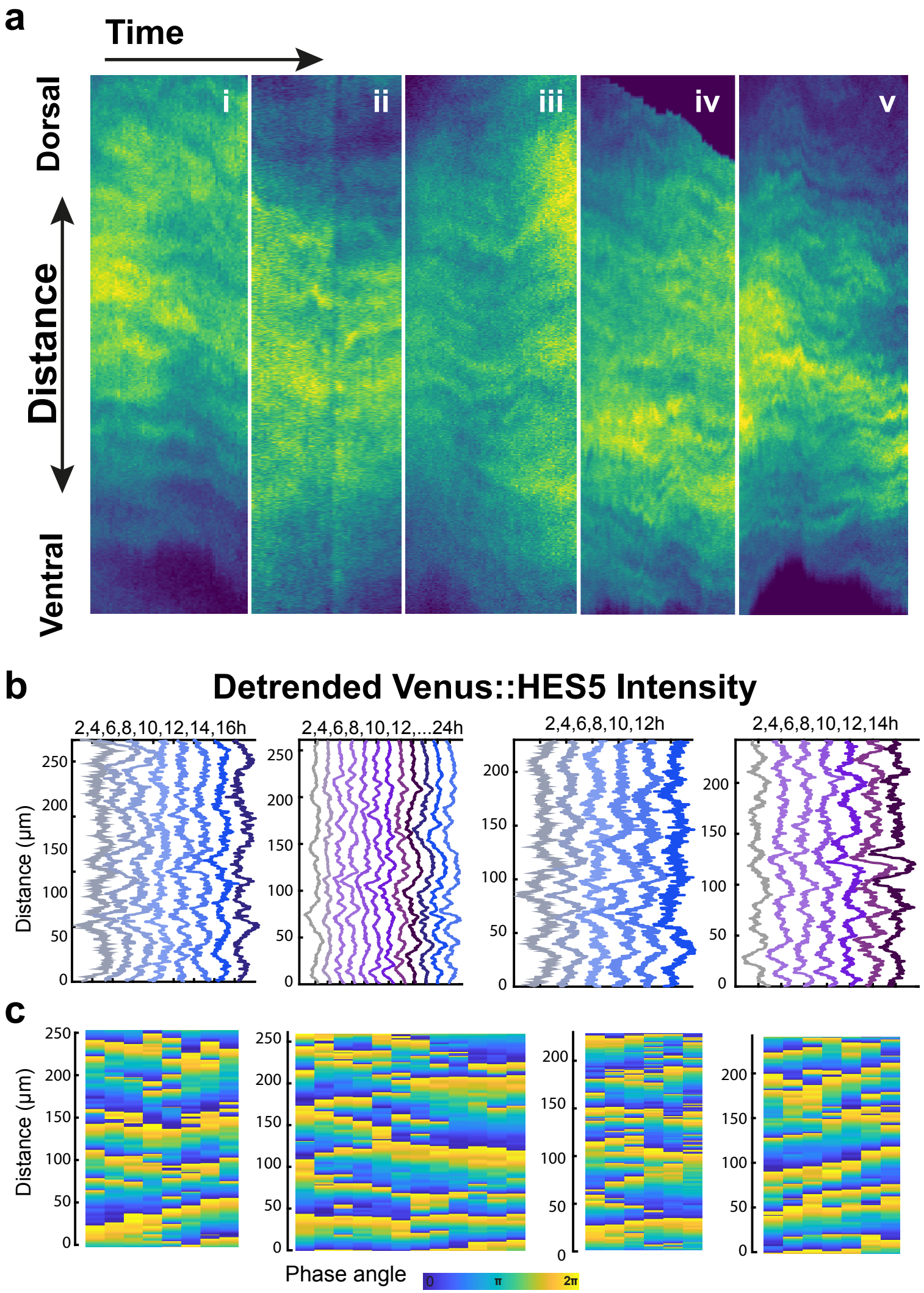

Supplementary Figure 4. Related to Figure 4.

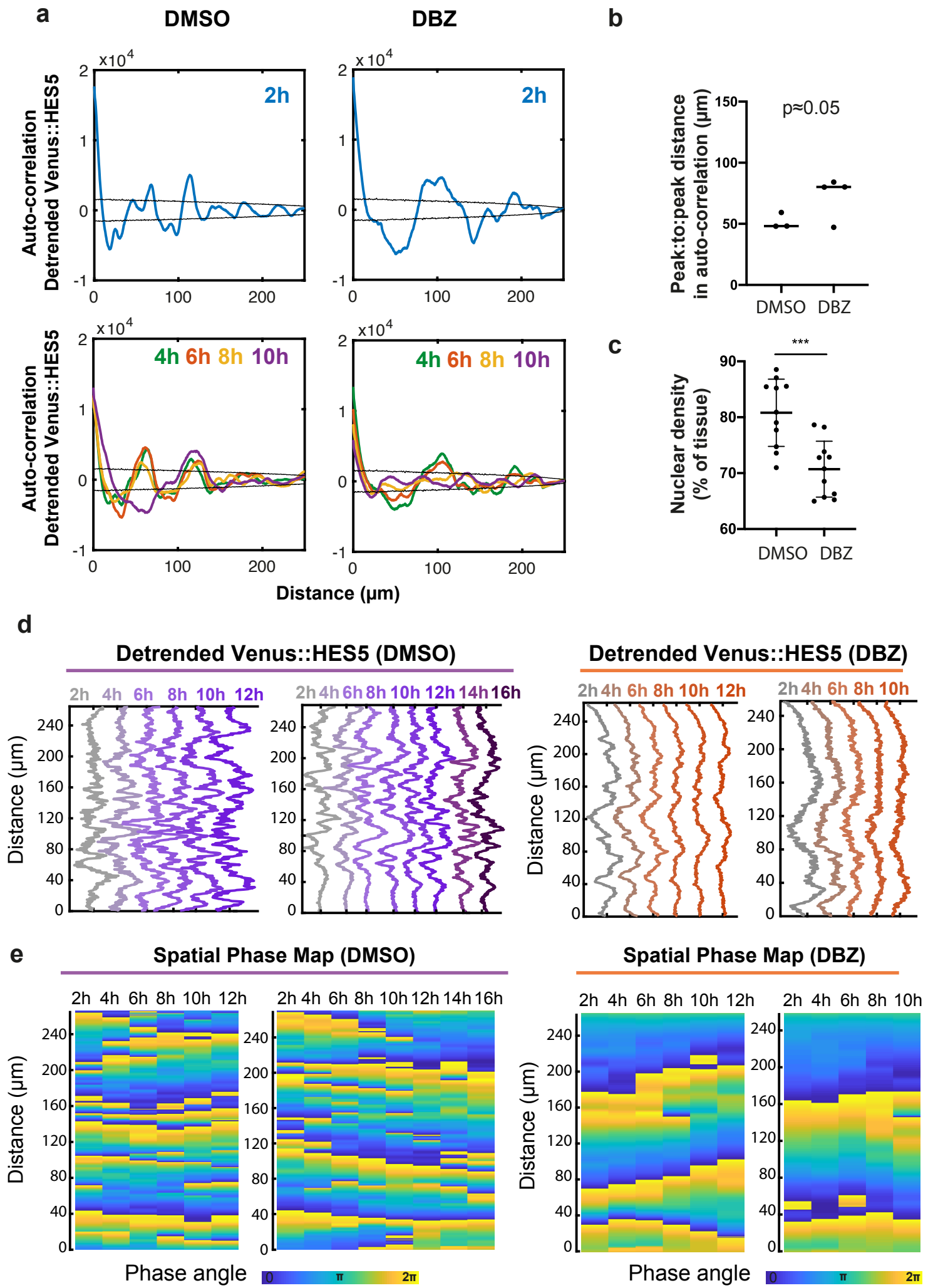

Supplementary Figure 5. Related to Figure 5.

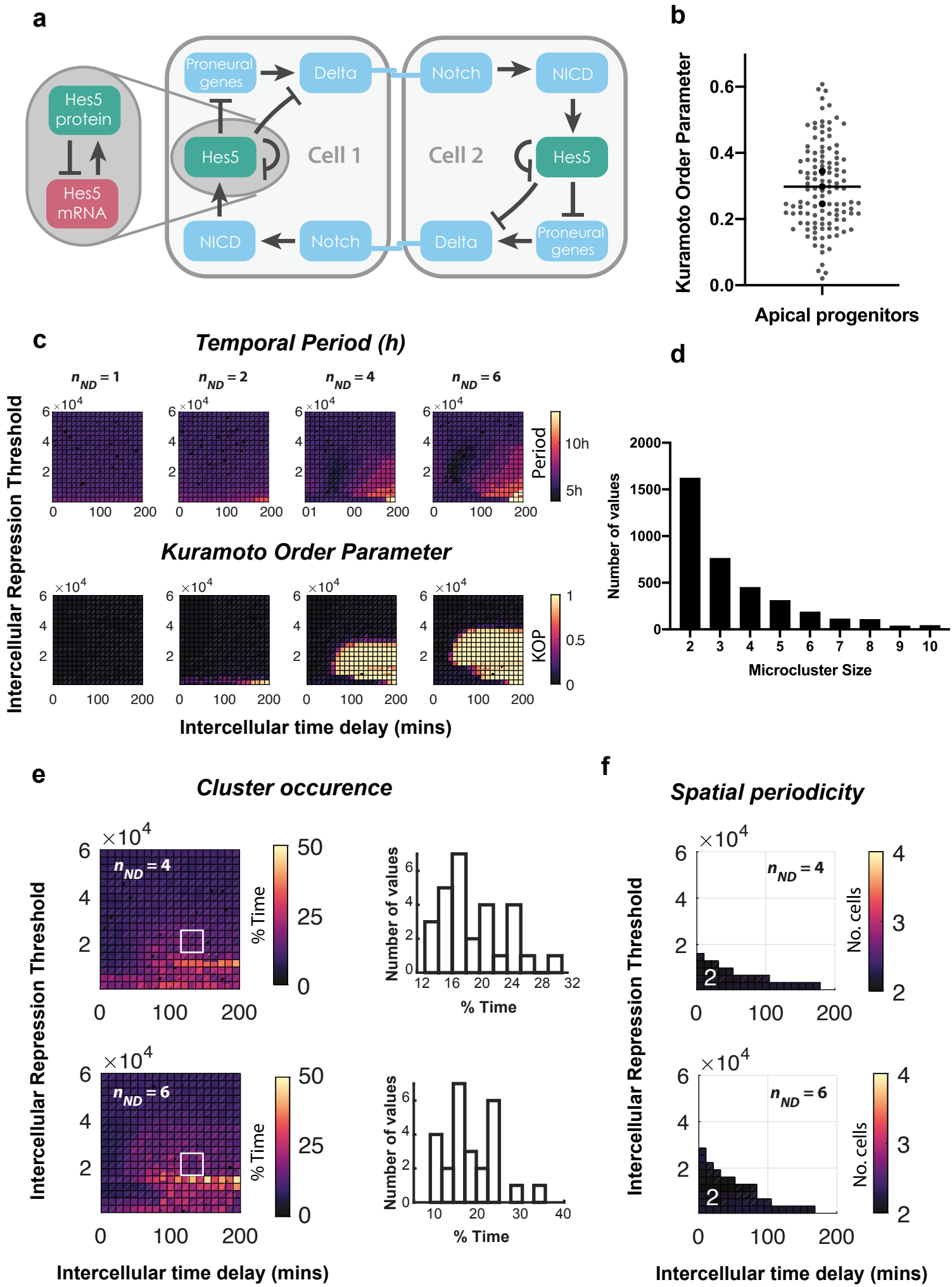

Supplementary Figure 6. Related to Figure 6.

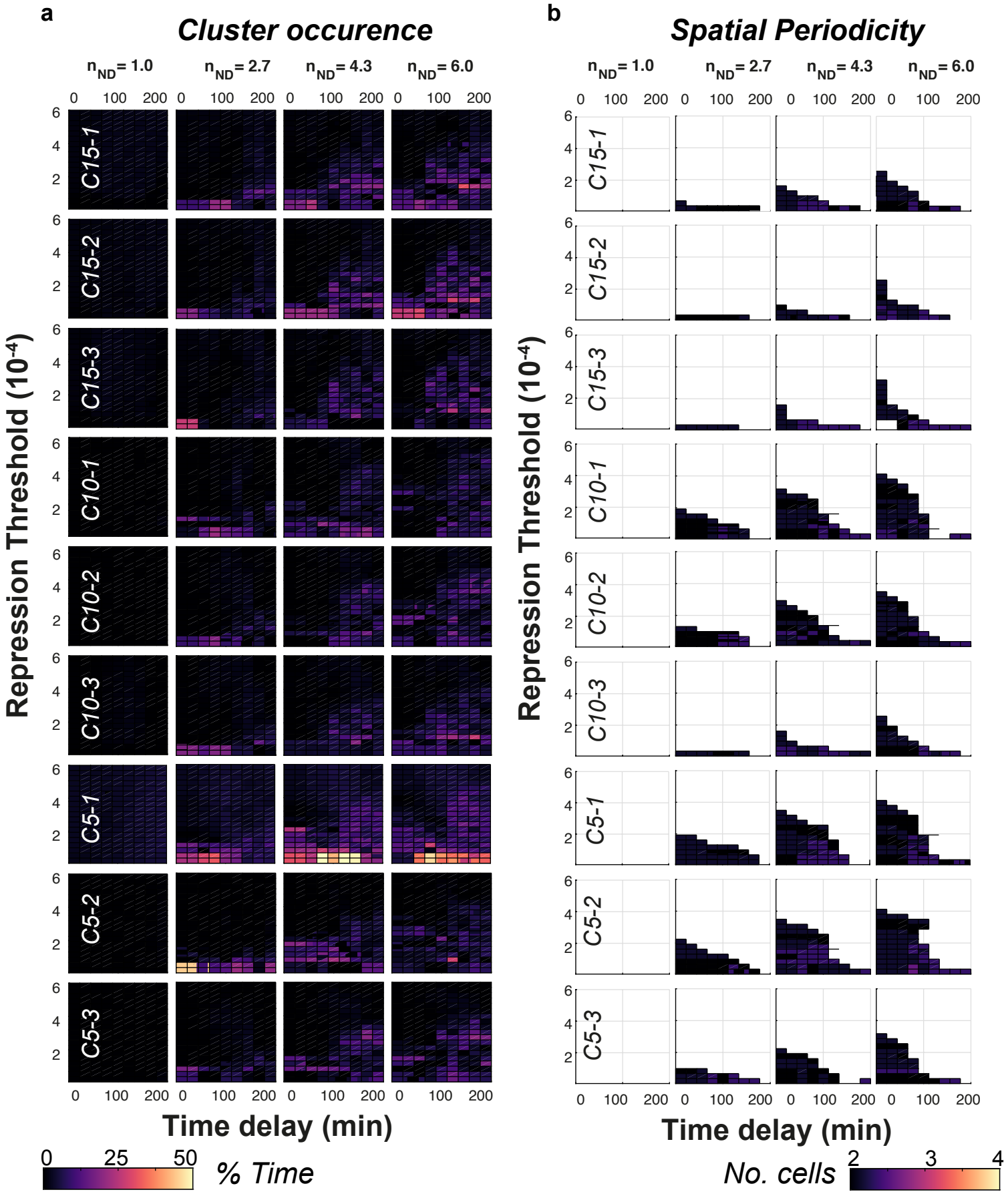

Supplementary Figure 7 . Related to Fig 7.

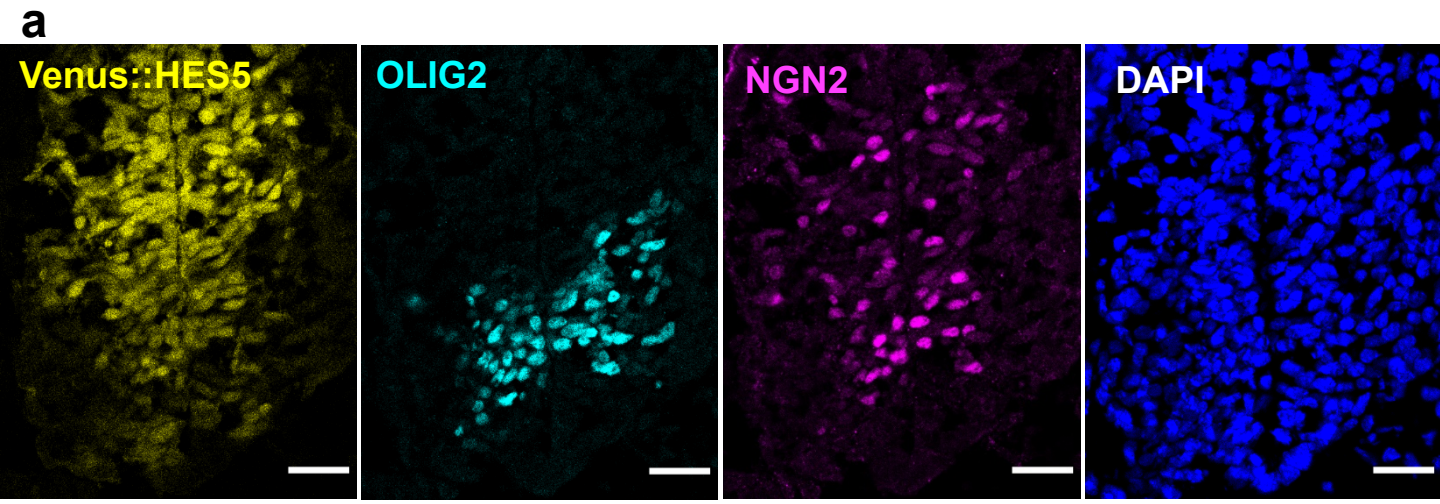

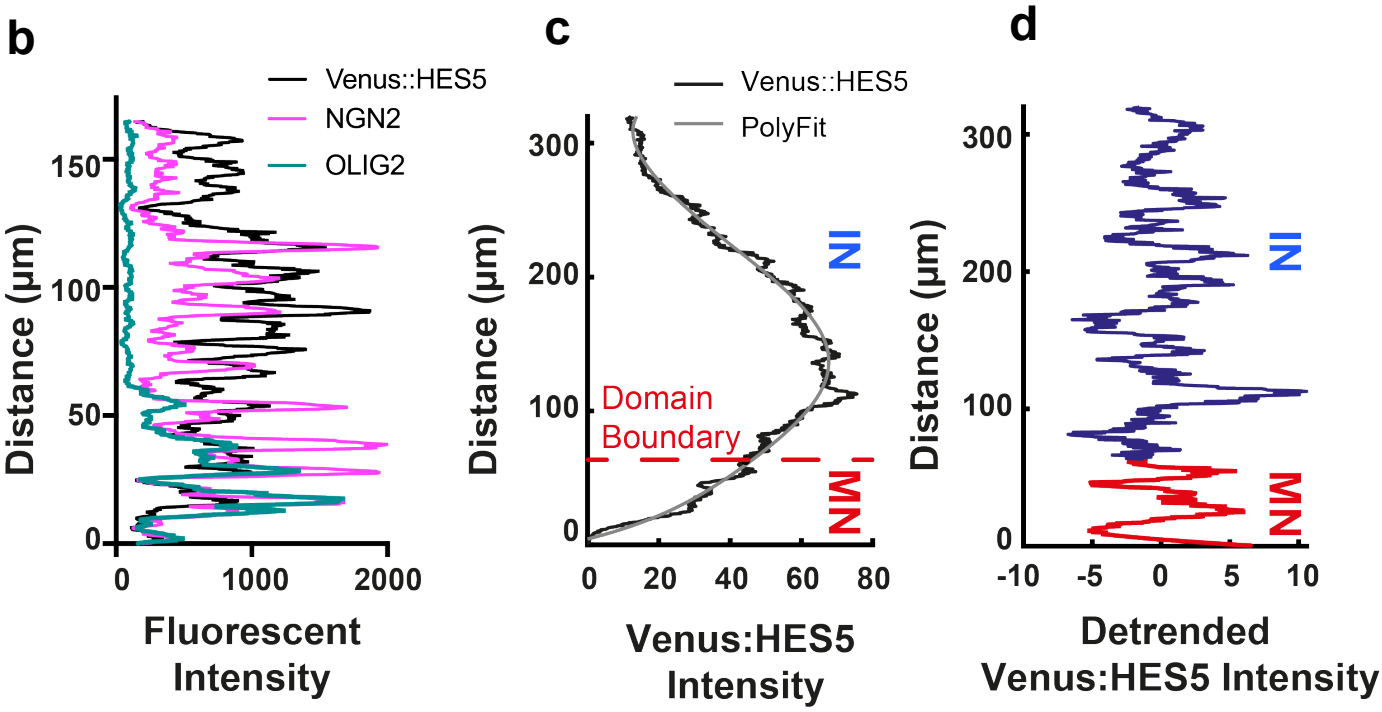

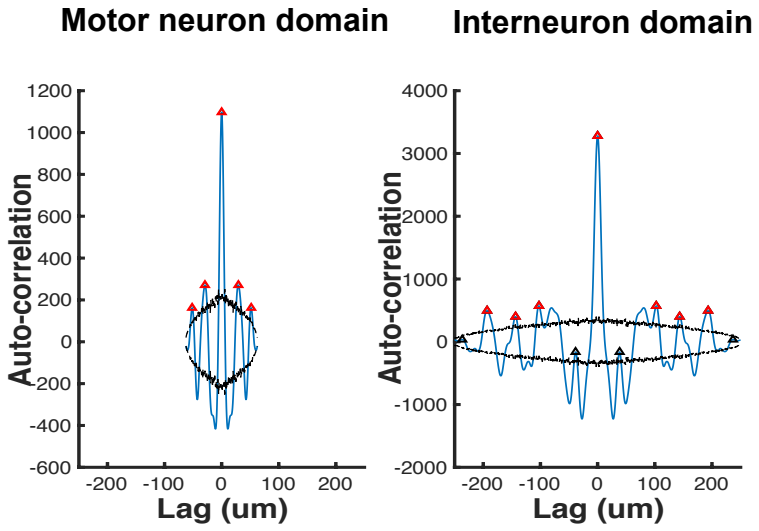

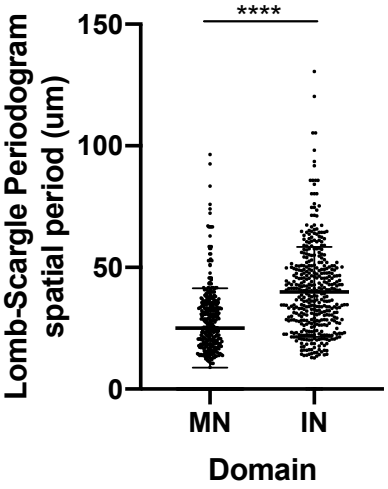

		Single-cell parameters							Multicellular parameters		
		Transcription rate	Translation rate	Repression threshold	Self-repression time delay	Self-repression Hill coefficient	mRNA degradation rate	Protein degradation rate	Intercellular repression threshold	Intercellular time delay	Intercellular Hill coefficient
Coherence	Parameter set name	α_m (min⁻¹)	α_p (min⁻¹)	P_{H0} (# of proteins)	τ_H (min)	n_H	μ_m (min⁻¹)	μ_p (min⁻¹)	P_{ND0} (# of proteins)	τ_{ND} (min)	n_{ND}
15%	**Main**	**0.8**	**26.4**	**25088**	**20**	**3.6**	$\frac{ln(2)}{30}$	$\frac{ln(2)}{90}$	$0-60000$	$0-200$	$1-6$
	C15-1	8.2	8.6	17914	23	2.7					
	C15-2	26.9	9.4	10902	20	2.6					
	C15-3	7.3	26.9	10733	24	2.3					
10%	C10-1	1.3	13.7	47482	36	2.6					
	C10-2	2.0	11.6	35319	19	2.5					
	C10-3	8.0	13.5	10255	19	2.0					
5%	C5-1	0.7	18.5	54656	38	2.6					
	C5-1	2.0	5.8	66657	28	2.1					
	C5-1	2.5	8.8	26823	22	2.0					